Contribution of the QCD Θ-term to the nucleon electric dipole moment

Tanmoy Bhattacharya,[1,*] Vincenzo Cirigliano,[1,†] Rajan Gupta,[1,‡] Emanuele Mereghetti,[1,§] and Boram Yoon[2,¶]

[1]*Los Alamos National Laboratory, Theoretical Division T-2, Los Alamos, New Mexico 87545, USA*
[2]*Los Alamos National Laboratory, Computer Computational and Statistical Sciences, CCS-7, Los Alamos, New Mexico 87545, USA*

(Received 15 February 2021; accepted 30 April 2021; published 10 June 2021)

We present a calculation of the contribution of the Θ-term to the neutron and proton electric dipole moments using seven $2+1+1$-flavor highly improved staggered quark ensembles. We also estimate the topological susceptibility for the $2+1+1$ theory to be $\chi_Q = (66(9)(4)\ \mathrm{MeV})^4$ in the continuum limit at $M_\pi = 135$ MeV. The calculation of the nucleon three-point function is done using Wilson-clover valence quarks. The $\not{C}\not{P}$ form factor F_3 is calculated by expanding in small Θ. We show that lattice artifacts introduce a term proportional to a that does not vanish in the chiral limit, and we include this in our chiral-continuum fits. A chiral perturbation theory analysis shows that the $N(\mathbf{0})\pi(\mathbf{0})$ state should provide the leading excited-state contribution, and we study the effect of such a state. Detailed analysis of the contributions to the neutron and proton electric dipole moment using two strategies for removing excited-state contamination are presented. Using the excited-state spectrum from fits to the two-point function, we find d_n^Θ is small, $|d_n^\Theta| \lesssim 0.01\bar{\Theta}\ \mathrm{e}\cdot\mathrm{fm}$, whereas for the proton we get $|d_p^\Theta| \sim 0.02\bar{\Theta}\ \mathrm{e}\cdot\mathrm{fm}$. On the other hand, if the dominant excited-state contribution is from the $N\pi$ state, then $|d_n^\Theta|$ could be as large as $0.05\bar{\Theta}\ \mathrm{e}\cdot\mathrm{fm}$ and $|d_p^\Theta| \sim 0.07\bar{\Theta}\ \mathrm{e}\cdot\mathrm{fm}$. Our overall conclusion is that present lattice QCD calculations do not provide a reliable estimate of the contribution of the Θ-term to the nucleon electric dipole moments, and a factor of 10 higher statistics data are needed to get better control over the systematics and possibly a 3σ result.

DOI: 10.1103/PhysRevD.103.114507

I. INTRODUCTION

The permanent electric dipole moments (EDMs) of nondegenerate states of elementary particles, atoms and molecules are very sensitive probes of *CP* violation ($\not{C}\not{P}$). Since the EDMs are necessarily proportional to the particle's spin, and under time reversal the direction of spin reverses but the electric dipole moment does not, a nonzero measurement confirms *CP* violation assuming *CPT* is conserved. Of the elementary particles, atoms and nuclei that are being investigated, the electric dipole moments of the neutron (nEDM) and the proton (pEDM) are the simplest quantities for which lattice QCD can provide the theoretical part of the calculation needed to connect the experimental bound or value to the strength of $\not{C}\not{P}$ in a given theory [1,2].

EDMs can shed light on one of the deepest mysteries of the observed Universe, the origin of the baryon asymmetry: the Universe has $6.1^{+0.3}_{-0.2} \times 10^{-10}$ baryons for every black-body photon [3], whereas in a baryon symmetric universe, we expect no more than about 10^{-20} baryons and anti-baryons for every photon [4]. It is difficult to include such a large excess of baryons as an initial condition in an inflationary cosmological scenario [5]. The way out of the impasse lies in generating the baryon excess dynamically during the evolution of the Universe. But, if the matter-antimatter symmetry was broken post inflation and reheating, then one is faced with Sakharov's three necessary conditions [6] on the dynamics: the process has to violate baryon number, evolution has to occur out of equilibrium, and charge conjugation and *CP* invariance have to be violated.

CP violation exists in the electroweak sector of the standard model (SM) of particle interactions due to a phase in the Cabibbo-Kobayashi-Maskawa (CKM) quark mixing matrix [7] and possibly due to a similar phase in the Pontecorvo-Maki-Nakagawa-Sakata matrix in the leptonic sector [8,9]. The effect of these on nEDM and pEDM is,

*tanmoy@lanl.gov
†cirigliano@lanl.gov
‡rajan@lanl.gov
§emereghetti@lanl.gov
¶boram@lanl.gov

however, small: that arising from the CKM matrix is about $O(10^{-32})$ $e\,$cm [10–12], much smaller than the current 90% confidence level (C.L.) experimental bound[1] $d_n < 1.8 \times 10^{-26}$ $e\,$cm [13] and than the reach of ongoing experiments, $d_n < 3.4 \times 10^{-28}$ $e\,$cm at 90% confidence [15].

In principle, the SM has an additional source of CP violation arising from the effect of QCD instantons. The presence of these localized finite action nonperturbative configurations in a non-Abelian theory leads to inequivalent quantum theories defined over various "Θ" vacua [16,17]. Because of asymptotic freedom, all nonperturbative configurations including instantons are strongly suppressed at high temperatures [18,19] where baryon number violating processes occur. Because of this, CP violation due to such vacuum effects does not lead to appreciable baryon number production [20]. Nonetheless, understanding the contribution of such a term to the nucleon EDM is very important for two reasons. First, the Θ term constitutes a "background" contribution to all hadronic EDMs that needs to be understood before one can claim discovery of new sources of CP violation through nucleon or hadronic EDM measurements; and second, besides generating higher-dimensional CP-odd operators, new sources of CP violation beyond the Standard Model (BSM) also generate a so-called "induced Θ-term" [1,21,22] if one assumes that the Peccei-Quinn mechanism is at work [23]. Therefore, in the large class of viable models of CP violation that incorporate the Peccei-Quinn mechanism, quantifying the contribution of the induced Θ to the nucleon EDM (operationally, the calculation is the same as in the first case) is essential to bound or establish such sources of CP violation.

Until recently, the calculation of hadronic matrix elements needed to connect nucleon EDMs to SM and BSM sources of CP violation relied on chiral symmetry supplemented by dimensional analysis [24–32] or QCD sum rules [1,22,33–36], both entailing large theoretical errors. Large-scale simulations of lattice QCD provide a first-principles method for calculating these matrix elements with controlled uncertainties. Several groups have reported results of lattice QCD calculations of the neutron EDM induced by the QCD Θ-term [37–44] and by higher-dimensional operators, such as the quark EDM [45,46] and at a more exploratory level the quark chromo-EDM [47–49]. In this paper, we present a new calculation of the contribution of the Θ-term to the nEDM and pEDM and show that the statistical and systematic uncertainties are still too large to extract reliable estimates.

[1]The slightly stronger 95% C.L. bounds $d_n < 1.6 \times 10^{-26}$ $e\,$cm and $d_p < 2.0 \times 10^{-25}$ $e\,$cm can be obtained from the experimental limit on the ^{199}Hg [14] EDM, assuming that nucleon EDMs are the dominant contributions to the nuclear EDM.

This paper is organized as follows: In Sec. II, we describe our notation by introducing the Lagrangian with $\not{C}\not{P}$ due to the Θ-term and the needed matrix elements. In Sec. III, we describe the decomposition of the matrix elements into the electromagnetic form factors. Section IV provides the lattice parameters used in the calculations. In Sec. V, we present the implementation of the gradient flow scheme, and in Sec. VI the calculation of the topological susceptibility. Section VII describes the methodology for extracting the $\not{C}\not{P}$ phase α from the two-point function, This phase, specific to the nucleon interpolating operator used, controls the CP transformation of the asymptotic nucleon state. Section VIII describes the calculation strategy for obtaining the form factors when this phase α is nonzero and gives the formulas used to extract the $\not{C}\not{P}$ form factor F_3 from the matrix elements. In Sec. IX, we discuss the extraction of $F_3(q^2)$ and the removal of the excited-state contamination. The extrapolation of $F_3(q^2)$ to $q^2 = 0$ is presented in Sec. X. Section XI discusses the lattice-spacing artifacts. Our results with the excited-state spectrum taken from the two-point function are presented in Sec. XII and those with an $N\pi$ excited state in Sec. XIII. These results are compared to previous calculations in Sec. XIV. Conclusions are presented in Sec. XV. Further details on the connection between Minkowski and Euclidean notation, the extraction of the form factors, the chiral extrapolation, excited-state contamination, and the $O(a)$ corrections in the Wilson-clover theory are presented in five appendixes.

II. THE QCD Θ-TERM

QCD allows for the existence of a P and T (and $\not{C}\not{P}$ if CPT is conserved) violating dimension-four operator, i.e., the Θ-term. In its presence, the QCD Lagrangian density in Euclidean notation becomes

$$\mathcal{L}_{\rm QCD} \to \mathcal{L}_{\rm QCD}^{\not{C}\not{P}} = \mathcal{L}_{\rm QCD} + i\Theta \frac{G^a_{\mu\nu}\tilde{G}^a_{\mu\nu}}{32\pi^2}, \tag{1}$$

where $G^a_{\mu\nu}$ is the chromo-field strength tensor, $\tilde{G}^a_{\mu\nu} = \frac{1}{2}\epsilon_{\mu\nu\lambda\delta}G^{a\lambda\delta}$ is its dual, and Θ is the coupling.[2] $G_{\mu\nu}\tilde{G}_{\mu\nu}$ is a total derivative of a gauge-variant current and its space-time integral gives the topological charge

$$Q = \int d^4x \frac{G^a_{\mu\nu}\tilde{G}^a_{\mu\nu}}{32\pi^2}. \tag{2}$$

[2]Throughout the paper, we work in Euclidean space, using q for the Euclidean 4-momentum and Q for the topological charge. The gauge field includes a factor of the strong coupling, g, so that the kinetic term is $G^a_{\mu\nu}G^a_{\mu\nu}/4g^2$. Also, our conventions for connecting the Euclidean and Minkowski metrics are given in Appendix A.

Nonzero values of Q are tied to the topological structure of QCD and the $U(1)$ axial anomaly. In addition, higher dimension operators that arise due to novel $\not{CP}$ couplings at the TeV scale generate this term under renormalization in a hard cutoff scheme like lattice regularization or gradient flow [45]. Also, BSM models in which the Peccei-Quinn mechanism is operative induce such a term [1].

Under a chiral transformation, one can rotate Θ into a complex phase of the quark matrix and vice versa. It is, therefore, necessary to work with the convention independent $\bar{\Theta} = \Theta + \mathrm{ArgDet}M_q$, which includes both Θ from all sources and the overall phase of the quark matrix M_q. Since the argument of the determinant is ill defined when it is zero, all physical effects of $\bar{\Theta}$ vanish in the presence of even a single massless quark flavor.

If the overall $\bar{\Theta}$ is nonzero, then this operator would induce an nEDM d_n of size

$$d_n = \bar{\Theta}X, \tag{3}$$

$$X \equiv \lim_{q^2 \to 0} \frac{F_3(q^2)}{2M_N\bar{\Theta}}. \tag{4}$$

Here X is obtained from the $\not{CP}$ part of the matrix element of the electromagnetic vector current within the neutron state in the presence of the Θ-term and F_3 is the $\not{CP}$ violating form factor defined in Eq. (6). At the leading order, F_3 is obtained from

$$\langle N|J_\mu^{\mathrm{EM}}|N\rangle|^{\bar{\Theta}} \approx \langle N|J_\mu^{\mathrm{EM}}|N\rangle|^{\bar{\Theta}=0} - i\bar{\Theta}\left\langle N\left|J_\mu^{\mathrm{EM}}\int d^4x \frac{G_{\mu\nu}^a\tilde{G}_{\mu\nu}^a}{32\pi^2}\right|N\right\rangle, \tag{5}$$

where we have assumed that the $\bar{\Theta}$-term is the only source of $\not{CP}$. In other words, X provides the connection between the $\not{CP}$ coupling ($\bar{\Theta}$) and the nEDM (d_n). Using the leading order form, instead of inserting $\exp i\bar{\Theta}Q$, improves the signal-to-noise ratio.

At present, the upper bound on the nEDM, $|d_n| < 1.8 \times 10^{-26}$ e cm (90% C.L.) [13], is used along with an estimate $X \sim (2.50 \pm 1.25) \times 10^{-16}$ e cm [1] to set a limit on the size of $\bar{\Theta} \lesssim 10^{-10}$. This is an unnaturally small number. One solution to this unnaturalness is the dynamical tuning of $\bar{\Theta} = 0$ using the Peccei-Quinn mechanism[3] [23].

Our goal is to calculate X using lattice QCD, which multiplied by the cumulative value, $\bar{\Theta}$, from all sources (SM or BSM), gives the full contribution to nEDM from the dimension-4 $G\tilde{G}$ operator in Eq. (1). Knowing X will allow current and future bounds on (or measured value of) d_n to more stringently constrain or pin down $\bar{\Theta}$.

[3]The Peccei-Quinn mechanism relaxes $\bar{\Theta}$ dynamically to Θ_{ind}, the point where the effective potential achieves its minimum. In the absence of other sources of CP violation in the theory, $\Theta_{\mathrm{ind}} = 0$.

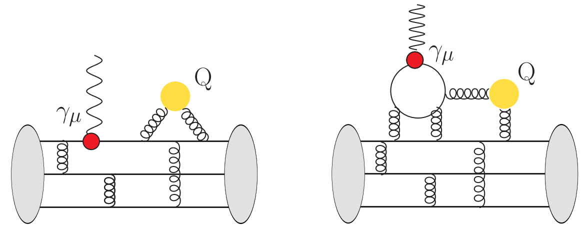

FIG. 1. The connected (left) and disconnected (right) diagrams with the insertion of the bilinear vector current (red filled circle) in the nucleon two-point function. The signal is given by the correlation between this three-point function and the topological charge shown by the filled yellow circle.

In the rest of the paper, all the analyses are carried out assuming that the only $\not{CP}$ coupling arises from the Θ-term, whose strength is $\bar{\Theta}$. Results are presented for $\bar{\Theta} = 0.2$, which we have checked is small enough so that $O(\bar{\Theta}^2)$ corrections are negligible for all quantities of interest (α and F_3 defined later).

The lattice calculation consists of the evaluation of the connected and disconnected diagrams shown in Fig. 1. The disconnected diagram gets contributions from all quark flavors in the loop—but their contributions to the CP-conserving form factors of the vector current are small [50]. In this work, we assume the same holds for the CP-violating ones and neglect these diagrams and their contribution to the electric dipole moment.

III. FORM FACTOR OF THE ELECTROMAGNETIC CURRENT

The parameterization of the matrix element of the electromagnetic current, $J_\mu^{\mathrm{EM}}(q)$, defined in Eq. (5), within the nucleon state in terms of the most general set of form factors consistent with the symmetries of the theory is

$$\begin{aligned}\langle N(p', s')|J_\mu^{\mathrm{EM}}|N(p,s)\rangle_{\not{CP}}^{\bar{\Theta}} &= \bar{u}_N(p',s')\Big[\gamma_\mu F_1(q^2) \\ &+ \frac{1}{2M_N}\sigma_{\mu\nu}q_\nu(F_2(q^2) - iF_3(q^2)\gamma_5) \\ &+ \frac{F_A(q^2)}{M_N^2}(\not{q}q_\mu - q^2\gamma_\mu)\gamma_5\Big]u_N(p,s),\end{aligned} \tag{6}$$

where M_N is the nucleon mass, $q = p' - p$ is the Euclidean 4-momentum transferred by the electromagnetic current, $\sigma_{\mu\nu} = (i/2)[\gamma_\mu, \gamma_\nu]$, and $u_N(p,s)$ represents the free neutron spinor of momentum p and spin s obeying $(i\not{p} + M_N)u_N(p,s) = 0$, with γ_4 implementing the parity operation on the asymptotic (i.e., free) state. Throughout, we work in Euclidean space and refer the reader to

TABLE I. Lattice parameters, nucleon mass M_N, number of configurations analyzed, and the total number of high precision (HP) and low precision (LP) measurements made. We also give the bin size (configurations per bin) used in the statistical analysis of two- and three-point functions. The last column gives the topological susceptibility χ_Q calculated at flow time $\tau_{gf} = 0.68$ fm and with a bin size of 20 configurations. The ensembles $a06m310$ and $a06m220$ have been used only for the calculation of χ_Q, and 861 configurations were used to calculate χ_Q on the $a06m135$ ensemble.

Ensemble ID	a [fm]	$M_\pi^{\rm val}$ [MeV]	$L^3 \times T$	$M_\pi^{\rm val} L$	τ/a	aM_N	$N_{\rm conf}$	Configurations per bin	N_{HP}	N_{LP}	$\chi_Q^{1/4}$ [MeV]
$a12m310$	0.1207(11)	310.2(2.8)	$24^3 \times 64$	4.55	$\{8, 10, 12\}$	0.6660(27)	1013	8	4052	64832	145.9(2.7)
$a12m220$	0.1184(09)	227.9(1.9)	$32^3 \times 64$	4.38	$\{8, 10, 12\}$	0.6122(25)	1000	8	4000	64000	145.3(2.4)
$a12m220L$	0.1189(09)	227.6(1.7)	$40^3 \times 64$	5.49	$\{8, 10, 12\}$	0.6125(21)	1000	8	4000	128000	141.3(2.5)
$a09m310$	0.0888(08)	313.0(2.8)	$32^3 \times 96$	4.51	$\{10, 12, 14\}$	0.4951(13)	2196	18	8784	140544	129.5(2.3)
$a09m220$	0.0872(07)	225.9(1.8)	$48^3 \times 96$	4.79	$\{10, 12, 14\}$	0.4496(18)	961	8	3844	123008	115.0(2.2)
$a09m130$	0.0871(06)	138.1(1.0)	$64^3 \times 96$	3.90	$\{10, 12, 14\}$	0.4204(23)	1289	11	5156	164992	106.8(1.7)
$a06m310$	0.0582(04)	319.3(5)	$48^3 \times 144$	4.5			970				127.0(5.5)
$a06m220$	0.0578(04)	229.2(4)	$64^3 \times 144$	4.4			1014				103.0(4.2)
$a06m135$	0.0570(01)	135.6(1.4)	$96^3 \times 192$	3.7	$\{16, 18, 20, 22\}$	0.2704(32)	453	9	1812	28992	89.3(2.8)

Appendix A for details on our conventions. F_1 and F_2 are the Dirac and Pauli form factors, in terms of which the Sachs electric and magnetic form factors are $G_E = F_1 - (q^2/4M_N^2)F_2$ and $G_M = F_1 + F_2$, respectively.[4] The anapole form factor F_A and the electric dipole form factor F_3 violate parity P; and F_3 violates CP as well. The zero momentum limit of these form factors gives the charges and dipole moments: The electric charge is $G_E(0) = F_1(0)$, the magnetic dipole moment is $G_M(0)/2M_N = (F_1(0) + F_2(0))/2M_N$, and the EDM is defined in Eq. (4).

In all the discussions in this paper, the current $J_\mu^{\rm EM}$ used is the renormalized local vector current $Z_V \sum_i e_i \bar\psi_i \gamma_\mu \psi_i$, where e_i is the electric charge of a quark with flavor i. The renormalization is carried out by taking ratios of all three-point fermion correlators with the lattice estimate of the vector charge, $g_V \equiv 1/Z_V$, which is given by the forward matrix element of $\bar\psi_i \gamma_4 \psi_i$. These ratios are constructed with identical source, sink, and current insertion positions and within the single jackknife loop used for the statistical analysis of the data to take advantage of error reduction due to correlated fluctuations.[5]

IV. LATTICE PARAMETERS

We present results on seven ensembles, whose parameters are specified in Table I. These were generated by the MILC Collaboration [51] using $2+1+1$ flavors of highly improved staggered quark (HISQ) action. For the construction of the nucleon correlation functions we use the clover-on-HISQ formulation that has been used extensively by us in the calculation of the nucleon charges and form factors as described in Refs. [52,53]. These ensembles cover three values of the lattice spacing, $a \approx 0.12$, 0.09 and 0.06 fm and three values of the pion mass $M_\pi \approx 315$, 220 and 130 MeV. Further details of the lattice parameters and methodology, statistics, and the interpolating operator used to construct the nucleon two- and three-point correlation functions can be found in Refs. [52,53].

V. TOPOLOGICAL CHARGE UNDER GRADIENT FLOW

We calculate the topological charge using the gradient flow scheme to implement operator renormalization and to reduce lattice discretization effects [41,54]. The primary advantage of the scheme is that at finite flow times,[6] i.e., for $\tau_{\rm gf} > 0$, the flow time provides an ultraviolet cutoff, and the continuum limit, $a \to 0$, of all operators built solely from gauge fields is finite. Moreover, since topological sectors arise dynamically as we take the continuum limit, the gradient flowed topological charge takes on integer values, and no renormalization is needed to convert it to a scheme that preserves this property; in particular, correlators of the topological charge are flow-time independent [54].

These statements are, however, not true at finite lattice spacing and volume. At small $\tau_{\rm gf}$, we get $O(a^2/\tau_{\rm gf}^2)$ artifacts. In Fig. 2, we show the distribution of the topological charge Q as a function of the flow time $\tau_{\rm gf}$

[4]We emphasize that we use q^2 for the *Euclidean* four-momentum squared that is denoted by Q^2 in our previous work and throughout the literature. As noted in Appendix A, it is the negative of the Minkowski four-momentum squared.

[5]This forward matrix element has very small excited-state contamination and, therefore, does not affect our excited-state fits at this level of precision.

[6]We use the notation $\tau_{\rm gf} \equiv \sqrt{8t}$ for the flow time, where t is the parameter in the flow equations in Ref. [54]. We used the Runge-Kutta integrator given in that reference for integrating the flow equations, with a step size of 0.01. Changing the step size to 0.002 changed the results on topological susceptibility by less than 0.2%.

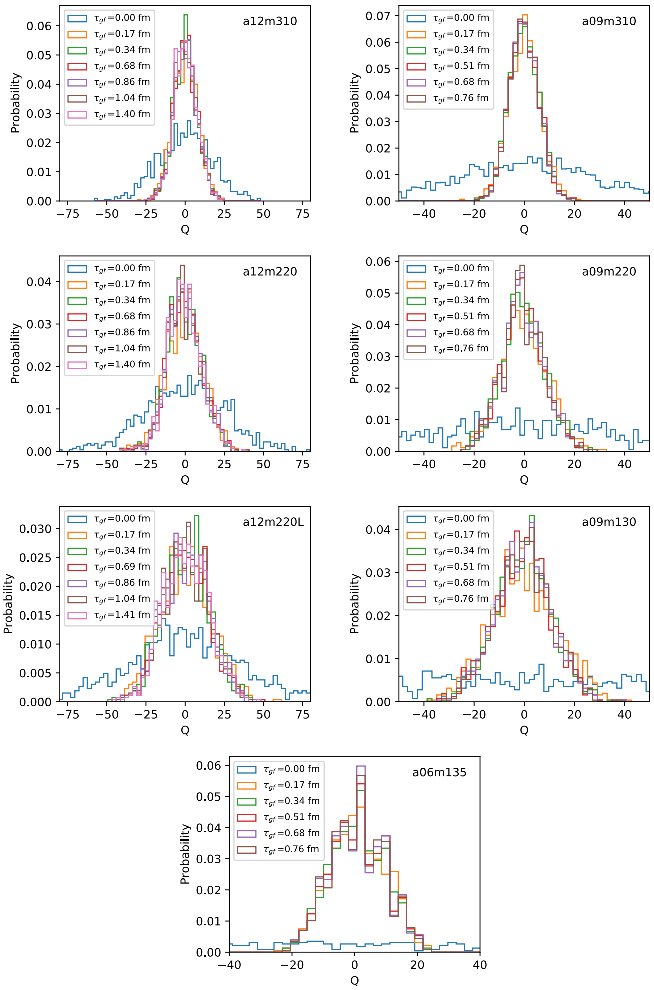

FIG. 2. The distribution of the topological charge Q as a function of the flow time τ_{gf}. The panels on the left (right) show data for the $a = 0.12$ fm ($a = 0.09$ fm) ensembles.

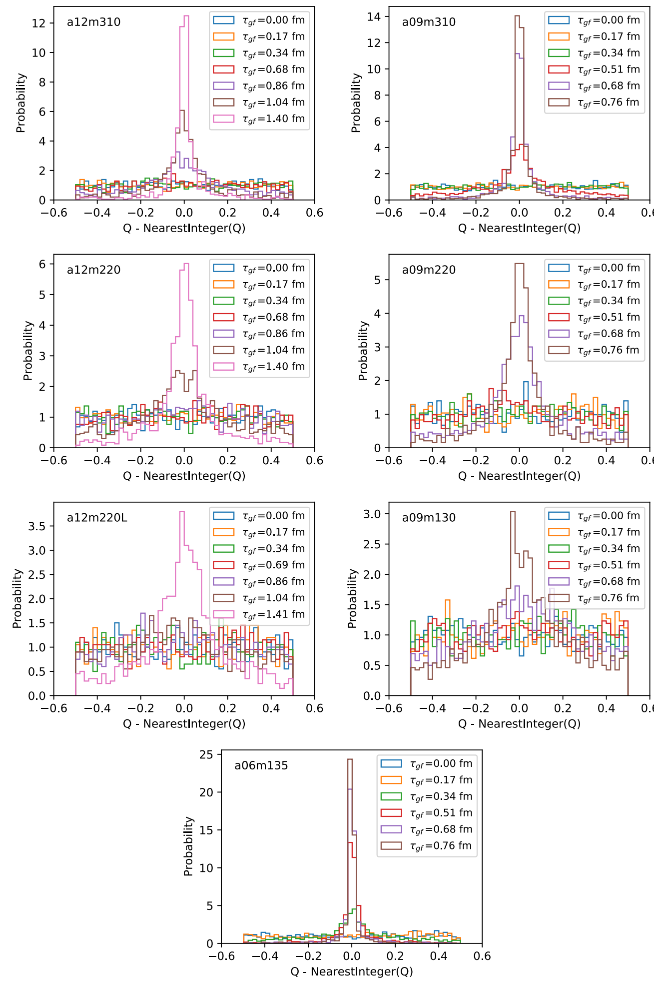

FIG. 3. The panels show the distribution of the difference, $Q - Q_{\mathrm{int}}$, of the measured Q from the nearest integer Q_{int}.

in physical units. Its distribution has stabilized by $\tau_{\mathrm{gf}} = 0.34$ fm for the $a = 0.12$ fm ensembles and by $\tau_{\mathrm{gf}} = 0.17$ fm for the $a = 0.09$ and 0.06 fm ensembles. The large values of Q that form the long tail of the distribution at $\tau_{\mathrm{gf}} = 0$ are smoothed out, indicating that they are lattice artifacts.

In Fig. 3, we show the distribution of the difference from the nearest integer. This distribution stabilizes more slowly and it is only by $\tau_{\mathrm{gf}} = 1.31$ fm ($\tau_{\mathrm{gf}} = 0.76$ fm) on the $a \approx 0.12$ fm ($a \approx 0.09$ and 0.06 fm) ensembles that the charges are close to integers. The relevant distribution important for the calculation of the nucleon correlation functions is, however, likely to be the distribution of Q shown in Fig. 2. To explore this, we show in Fig. 4 the value of F_3 as a function of τ_{gf} for the $a \approx 0.12$ and 0.09 fm ensembles and find that indeed the correlation functions, and thus F_3, do stabilize early but the τ_{gf} required for the coarser lattices is longer. Thus, to be conservative, the results presented below are obtained with flow times $\tau_{\mathrm{gf}}(a06) = 0.68$ fm, $\tau_{\mathrm{gf}}(a09) = 0.68$ fm and $\tau_{\mathrm{gf}}(a12) = 0.86$ fm, respectively.

In Fig. 5, we show the distribution of the nearest integer, Q_{int}, to the topological charge at $\tau_{\mathrm{gf}} \approx 1.4$ fm ($\tau_{\mathrm{gf}} = 0.76$ fm) on the $a \approx 0.12$ fm ($a \approx 0.09$ and 0.06 fm) ensembles, by which time the Q_{int} identified with a given configuration has stabilized. This distribution is approximately symmetric about zero as expected since $\langle Q \rangle = 0$, and no gaps are visible in the distribution. In Fig. 6, we show the autocorrelation function of Q versus the flow time. The data show no significant change after $\tau_{\mathrm{gf}} \gtrsim 0.3$ fm, so we can determine the autocorrelation from these data. We do not observe a long time freeze in Q in any of the ensembles analyzed as illustrated using the $a09m130$ and $a06m135$ ensembles at flow time $\tau_{\mathrm{gf}} = 0.68$ fm in Fig. 7. The autocorrelation is less than about ten configurations for all but the $a06m135$ ensemble. Based on this study, the bin size used in the single elimination jackknife procedure is given in Table I.

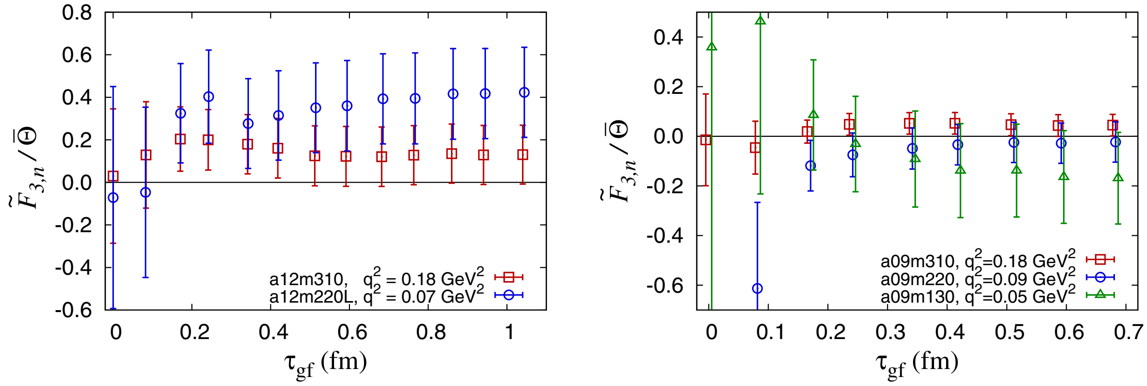

FIG. 4. Data for $\tilde{F}_{3,n}/\bar{\Theta}$, defined in Eq. (28), at the smallest value of q^2, respectively, on the $a12$ (left panel) and the $a09$ (right panel) ensembles. The estimates show no significant change after $\tau_{\rm gf} \approx 0.4$ fm on the $a09$ ensembles and $\tau_{\rm gf} \approx 0.6$ fm on the $a12$ ensembles.

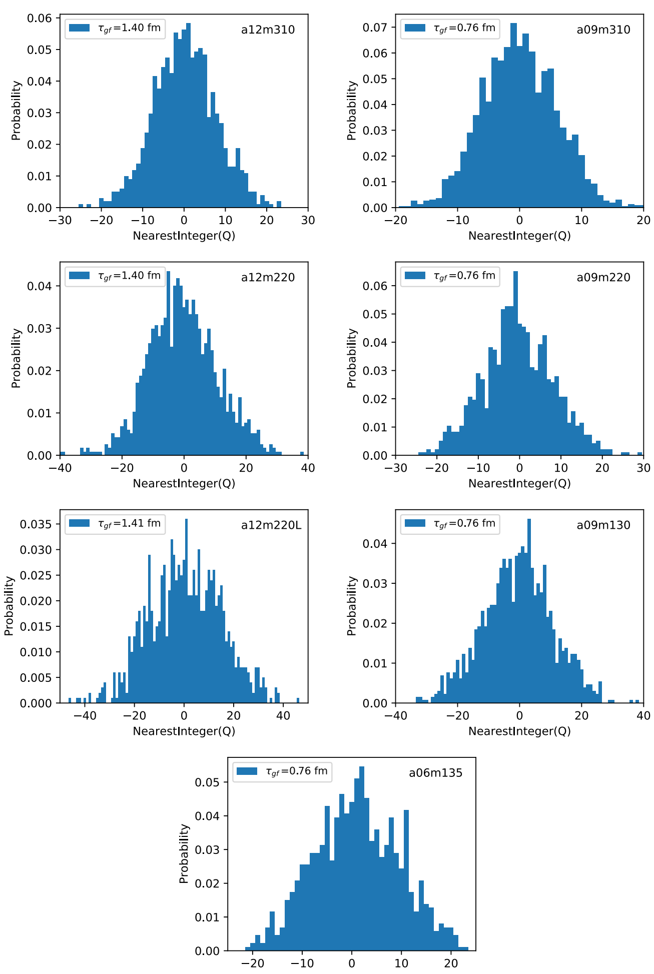

FIG. 5. The distribution of the nearest integer charge, $Q_{\rm int}$, associated with a given configuration at $\tau_{\rm gf} \approx 1.4$ fm ($a12$ ensembles) and 0.76 fm ($a09$ and $a06$ ensembles), by which time the $Q_{\rm int}$ identified with a given configuration has stabilized.

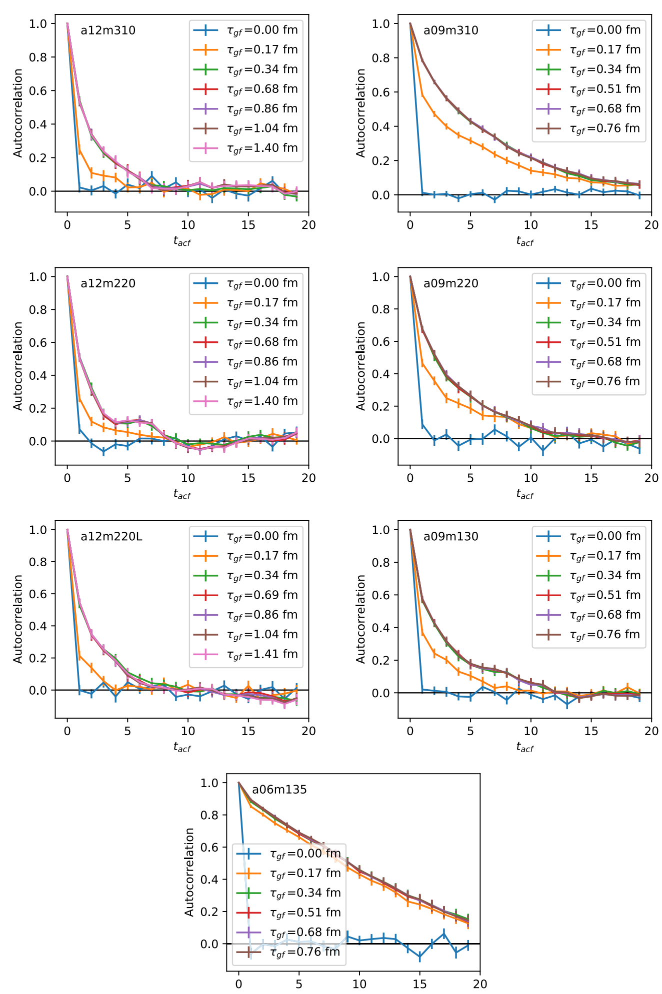

FIG. 6. The autocorrelation function for different values of the flow time. The data show that the long $\tau_{\rm gf}$ behavior stabilizes by $\tau_{\rm gf} = 0.34$ fm in all cases.

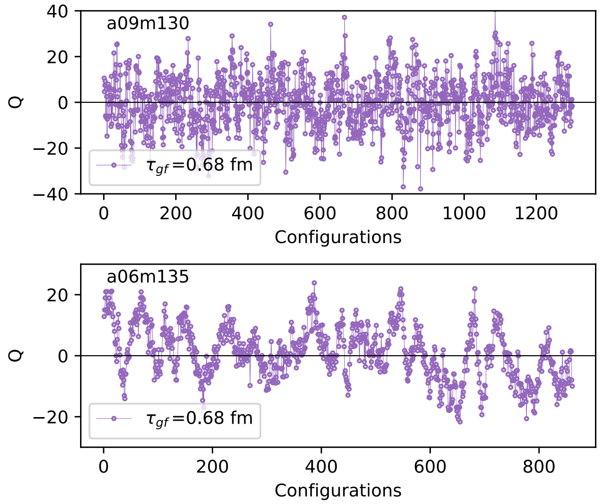

FIG. 7. The time history of Q on the $a09m130$ (upper) and $a06m135$ (lower) ensembles at $\tau_{\rm gf} = 0.68$ fm. While the autocorrelations increase as $a \to 0$, the data show no long-time freezing of the topological charge.

VI. TOPOLOGICAL SUSCEPTIBILITY

The topological susceptibility χ_Q is defined as

$$\chi_Q = \int d^4x \langle Q(x)Q(0)\rangle. \tag{7}$$

Its value in the pure gauge theory, $\chi_Q^{\rm quenched}$, is related to the mass of the η' meson in a theory with N_f light flavors in the chiral limit via the axial anomaly, viz., the Witten-Veneziano relation [55,56]

$$M_{\eta'}^2 \approx \frac{2N_f}{F_\pi^2}\chi_Q^{\rm quenched}, \tag{8}$$

where F_π is the pion decay constant in the convention where its physical value is about 92 MeV. Following Ref. [57], we can include the effects of the quark masses. Including $SU(3)$ breaking at leading order in χPT but neglecting the heavier quarks gives

$$\chi_Q^{\rm quenched} \approx \frac{F_\pi^2(M_{\eta'}^2 - M_\eta^2)}{6}\left(\sqrt{1 - \frac{32\delta_{K\pi}^2}{9}} + \frac{2\delta_{K\pi}}{3}\right),$$
$$\chi_Q^{\rm quenched} \approx \frac{F_\pi^2(M_{\eta'}^2 - M_\eta^2)}{6}\left(1 + 2\frac{M_\eta^2 - M_K^2}{M_{\eta'}^2 - M_\eta^2}\right), \tag{9}$$

where $\delta_{K\pi} \equiv (M_K^2 - M_\pi^2)/(M_{\eta'}^2 - M_\eta^2)$ is an $SU(3)$ breaking ratio. The two expressions, which can be derived independently, give $\chi_Q^{\rm quenched} \approx (172\ {\rm MeV})^4$ and $(179\ {\rm MeV})^4$ respectively, thus quantifying the accuracy of the expansion.

With dynamical fermions, however, the susceptibility should vanish in the chiral limit. For $SU(N_f)$ flavor group with finite but degenerate quark masses, it should behave as [58–60]

$$\frac{1}{\chi_Q} \approx \frac{1}{\chi_Q^{\rm quenched}} + \frac{2N_f}{M_\pi^2 F_\pi^2}. \tag{10}$$

For $N_f = 2$ light flavors and the strange quark, but neglecting the heavier quarks that give negligible corrections, leading order chiral perturbation theory (χPT) modifies this to

$$\frac{1}{\chi_Q} \approx \frac{1}{\chi_Q^{\rm quenched}} + \frac{4}{M_\pi^2 F_\pi^2}\left(1 - \frac{M_\pi^2}{3M_\eta^2}\right)^{-1}. \tag{11}$$

We calculate χ_Q on the $2+1+1$-flavor HISQ ensembles, which are $O(a)$ improved. The results are given in Table I. In addition to the seven ensembles used to calculate F_3, we include data from the $a06m310$ and $a06m220$ ensembles. We remind the reader that the MILC Collaboration has previously highlighted the issue of frozen topology on these ensembles [61], which is why we do not use them in the calculation of F_3.

As discussed in Sec. V, the topological susceptibility at finite flow time needs no renormalization and should be independent of flow time up to $O(a^2/\tau_{\rm gf}^2)$ effects. As shown in Fig. 8, this is true up to a small, almost linear, downward drift with increasing flow time. In Fig. 9, we compare the results on $a12m220$ and $a12m220L$ ensembles and show that this is a $\tau_{\rm gf}^2/L^2$ effect, where L is the lattice size.[7] At the flow times and volumes we use in the calculation, this is a small effect and therefore neglected.

To obtain χ_Q at $M_\pi = 135$ MeV and $a = 0$, we use the fit ansatz

$$\chi_Q(a, M_\pi) = c_1 a^2 + c_2 M_\pi^2 + c_3 a^2 M_\pi^2, \tag{12}$$

which assumes χ_Q is zero in the chiral-continuum limit. We do not find a viable χ^2/d.o.f. on including all nine data points. Reasonable fits are found on neglecting (i) all three $a \approx 0.12$ fm points and (ii) all three $a \approx 0.12$ fm and the $a06m310$ point. These two fits give $\chi_Q = [70(6)\ {\rm MeV}]^4$ and $\chi_Q = [63(9)\ {\rm MeV}]^4$, respectively, at $M_\pi = 135$ MeV. We take the average $\chi_Q = [66(9)(4)\ {\rm MeV}]^4$ as our best estimate, the larger of the two errors and an additional systematic uncertainty, which is half the difference. These results are in good agreement with the expected value $(79\ {\rm MeV})^4$, obtained using the physical meson masses and

[7]For asymmetric, $(T/a > L/a)$, lattices like ours, we expect the smaller spatial extent L/a to dominate the finite volume effect.

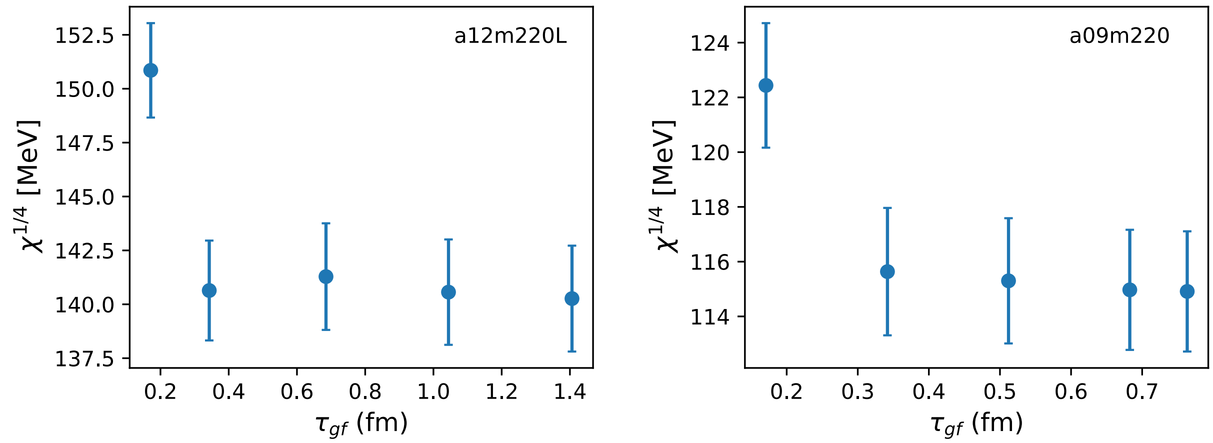

FIG. 8. Illustration of the flow-time dependence of the topological susceptibility at small flow times showing that it is almost independent of the flow time when the flow time is much larger than the lattice spacing.

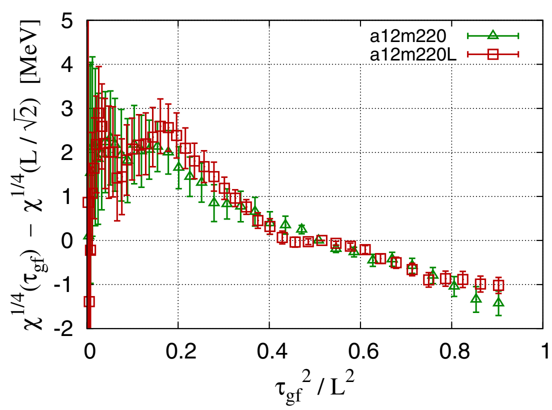

FIG. 9. Comparison of the flow-time dependence of the topological susceptibility at large flow times on two ensembles differing only in lattice volume, showing that the dependence is a finite size effect.

decay constants in Eqs. (9) and (11). The data and the fit case (i) are shown in Fig. 10.

VII. CALCULATION OF THE $\cancel{CP}$ PHASE α

In a field theory in which parity is not conserved, the definition of parity of a composite state, e.g., the neutron state, needs care [22,33,37]. To explain this, we start with the most general spectral decomposition of the time-ordered two-point nucleon correlator

$$\langle\Omega|\mathcal{T}N(\boldsymbol{p},\tau)\bar{N}(\boldsymbol{p},0)|\Omega\rangle = \sum_{i,s} e^{-E_i\tau}\mathcal{A}^*{}_i\mathcal{A}_i\mathcal{M}_i^s, \qquad (13)$$

where $\mathcal{A}_i$ is the amplitude for creating state i, E_i is its energy, the Euclidean time τ is the separation between the source and the sink, and, for notational convenience, we are assuming a discrete spectrum. A common choice on the lattice of the neutron interpolating operator N is

$$N \equiv \epsilon^{abc}\left[d^{a\mathrm{T}}C\gamma_5\frac{1+\gamma_4}{2}u^b\right]d^c, \qquad (14)$$

where $C=\gamma_2\gamma_4$ (the sign is conventional and does not affect the nucleon correlators we study; see Appendix A for details of our convention) is the charge conjugation matrix, a, b, and c are the color indices and u and d are the quark flavors. The 4×4 spinor matrix $\mathcal{M}_i^s$ in Eq. (13) depends on the state and the momentum $\boldsymbol{p}$. Its most general form consistent with Lorentz covariance is[8]

$$\sum_s \mathcal{M}_i^s = e^{i\alpha_i\gamma_5}\frac{(-i\not{p}_i + M_i)}{2E_i^p}e^{i\alpha_i^*\gamma_5} \qquad (15)$$

$$\equiv e^{i\alpha_i\gamma_5}\sum_s u_N^i(\boldsymbol{p},\boldsymbol{s})\bar{u}_N^i(\boldsymbol{p},\boldsymbol{s})e^{i\alpha_i^*\gamma_5}, \qquad (16)$$

where $p_i^4 \equiv iE_i$. It is clear that because of the presence of the phases α_i, the parity operator that transforms the spinor associated with the ith asymptotic state is $\mathcal{P}_{\alpha_i} \equiv e^{i\alpha_i\gamma_5}\mathcal{P}e^{-i\alpha_i\gamma_5}$, where $\mathcal{P}\equiv\eta\gamma_4$ is the usual parity operator for a particle with intrinsic parity η. The phases α_i depend on the realization of discrete symmetries: If the interpolating field is chosen such that $\mathcal{P}$ implements parity in the free theory, Im $\alpha_i = 0$ for a PT symmetric theory, Re $\alpha_i = 0$ for the CP symmetric theory, and $\alpha_i = 0$ for a P symmetric theory. For our case of only $\cancel{CP}$, all α_i are, therefore, real, which will be implicit except in Appendix B. It is important to note that the value of α_i depends on the interpolating operator N, the state, and the source of $\cancel{CP}$. Its value for the ground state can be extracted from the large τ behavior of the imaginary part of the nucleon two-point function. Consider

[8]Up to a possible extra factor of γ_5, which, however, is prohibited by PT symmetry in our calculations.

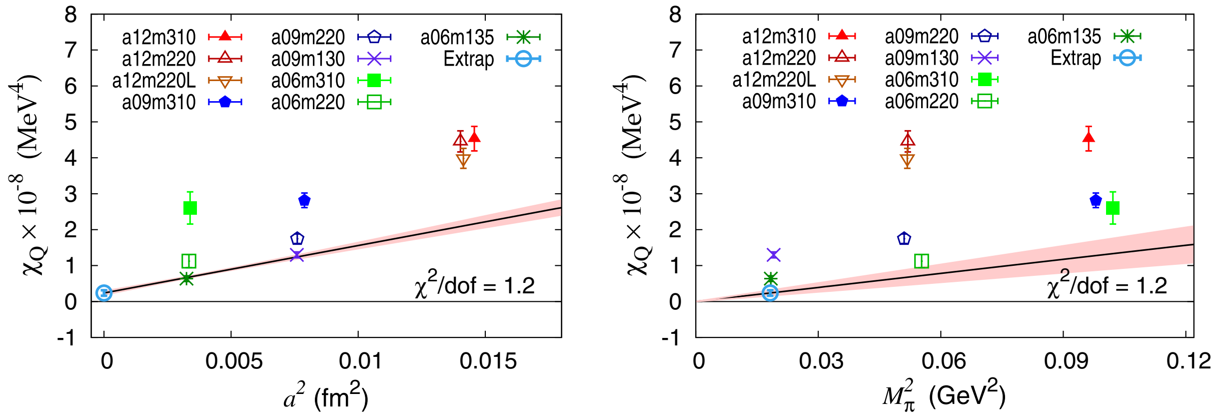

FIG. 10. Fits to the data for the topological susceptibility, χ_Q, using the ansatz given in Eq. (12).

$$r_\alpha(\tau) \equiv \frac{\mathrm{Im}C^P_{\mathrm{2pt}}(\tau)}{\mathrm{Re}C_{\mathrm{2pt}}(\tau)} \tag{17}$$

$$\equiv \frac{\mathrm{ImTr}[\gamma_5 \frac{1}{2}(1+\gamma_4)\langle N(\tau)\bar{N}(0)\rangle]}{\mathrm{ReTr}[\frac{1}{2}(1+\gamma_4)\langle N(\tau)\bar{N}(0)\rangle]} \tag{18}$$

$$= \frac{\sum_i M_i \sin(2\alpha_i)|\mathcal{A}_i|^2/(2E_i)e^{-E_i\tau}}{\sum_i (E_i + M_i\cos(2\alpha_i))|\mathcal{A}_i|^2/(2E_i)e^{-E_i\tau}}. \tag{19}$$

Keeping only the first two states one gets

$$r_\alpha(\tau) \approx \frac{M_0\sin(2\alpha_0)}{E_0 + M_0\cos(2\alpha_0)} \times \frac{1 + \frac{M_1E_0}{M_0E_1}\frac{\sin(2\alpha_1)}{\sin(2\alpha_0)}|\tilde{\mathcal{A}}_1|^2 e^{-(E_1-E_0)\tau}}{1 + \frac{(E_1+M_1\cos(2\alpha_1))E_0}{(E_0+M_0\cos(2\alpha_0))E_1}|\tilde{\mathcal{A}}_1|^2 e^{-(E_1-E_0)\tau}}, \tag{20}$$

where $\tilde{\mathcal{A}}_i = \mathcal{A}_i/\mathcal{A}_0$. At zero three-momentum ($E_i = M_i$) the above expression simplifies to

$$r_\alpha(\tau) \approx \tan\alpha_0 \times \frac{1 + \frac{\sin(2\alpha_1)}{\sin(2\alpha_0)}|\tilde{\mathcal{A}}_1|^2 e^{-(M_1-M_0)\tau}}{1 + \frac{\cos^2(\alpha_1)}{\cos^2(\alpha_0)}|\tilde{\mathcal{A}}_1|^2 e^{-(M_1-M_0)\tau}}. \tag{21}$$

We provide these formulas for the general case, without expanding to linear order in α_i, but checked explicitly that for the values of $\bar{\Theta}$ used in our calculation, we are in the linear regime. The results for $\alpha/\bar{\Theta}$ and $F_3/\bar{\Theta}$ can, however, show a tiny dependence on $\bar{\Theta}$ as a result. The data for r_α versus τ are shown in Fig. 11 for all seven ensembles. The α_0 for the ground state obtained from the two-state fit agrees with the plateau at large τ, where the lowest state dominates, and is independent of the momentum.

The ground-state value of α_0 for a neutron, denoted α_N, extracted using Eq. (21) depends on the mass gap $M_1 - M_0$. The same is true for the form factor F_3. In Appendix D, we present a chiral perturbation theory analysis showing that the lowest excited state that can contribute to the matrix element defined in Eq. (6) is the $N(0)\pi(0)$. We have therefore carried out the full analysis of the contribution of the Θ-term to the neutron EDM using two estimates of the mass gap. In the first, standard, case, the $M_1 - M_0$ is obtained from a three-state fit to the real part of the two-point function. In the second, the excited state is taken to be $N(0)\pi(0)$ with mass gap M_π. The values of these two mass gaps and the corresponding values of the phases obtained, α_N and $\alpha_N^{N\pi}$, are given in Table II.

VIII. THREE-POINT FUNCTIONS IN THE PRESENCE OF THE PHASE α

In the presence of the phase α_N for the ground-state nucleon [47], the most straightforward way to extract the matrix element of the electromagnetic current J_μ^{EM} within the neutron ground state in the presence of $\not{C}\not{P}$ is to calculate the correlation function

$$e^{-i\alpha_N\gamma_5}\langle\Omega|N(\boldsymbol{p}',\tau)J_\mu^{\mathrm{EM}}(\boldsymbol{q},t)\bar{N}(\boldsymbol{p},0)|\Omega\rangle|_{\not{C}\not{P}}e^{-i\alpha_N\gamma_5} \propto (-i\not{p}' + M_N)O^\mu(q)(-i\not{p} + M_N), \tag{22}$$

where $p' \equiv p + q$ and

$$O^\mu(q) \equiv \gamma^\mu F_1 + \frac{1}{2M_N}\sigma^{\mu\nu}q^\nu(F_2 - iF_3\gamma_5) + \frac{F_A}{M_N^2}(\not{q}q^\mu - q^2\gamma^\mu)\gamma_5. \tag{23}$$

Here, the current J_μ^{EM} is inserted at times t between the neutron source and sink operators located at time 0 and τ, and a sum over the spin labels is implicit. We also assume that t and τ are large enough that only the ground state dominates the correlation function. This form results from the realization that γ_4 remains the parity operator for the ground-state nucleon when working with the interpolating field defined to be $e^{-i\alpha_N\gamma_5}N$ instead of N in all correlation functions.

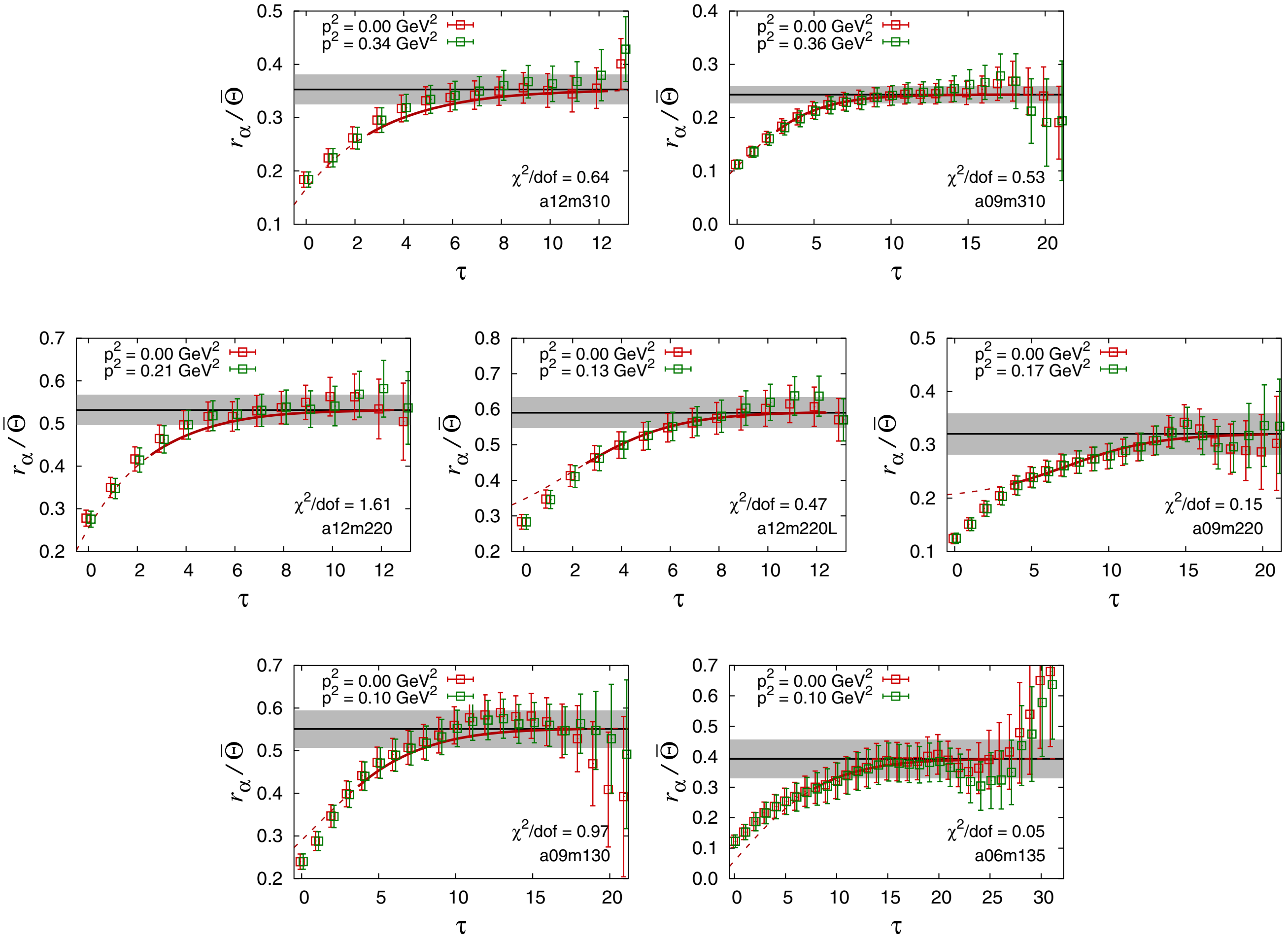

FIG. 11. The extraction of the phase $\alpha_N/\bar{\Theta}$ with $\bar{\Theta} = 0.2$ for the ground-state nucleon on the seven ensembles from the asymptotic value of r_α defined in Eq. (21) using the excited-state mass gap obtained from the real part of the two-point function given in Table II. It is a Lorentz scalar and independent of the momentum as confirmed by the lattice data. The χ^2/d.o.f. values presented are from fully correlated fits, except for the case of the $a09m220$ and $a06m135$ ensembles on which we use uncorrelated fits to avoid instabilities.

This approach, however, requires, evaluating the full 4×4 matrix of three-point correlation functions. In our calculation, we have implemented the spin projection using

$$\mathcal{P}_{3\mathrm{pt}} \equiv \frac{1}{2}(1+\gamma_4)(1+i\gamma_5\gamma_3), \tag{24}$$

so the contribution of a nonzero α_N has to be incorporated at the time of the decomposition of the matrix element into the form factors. As discussed in Appendix B, by taking a suitable ratio of three- and two-point functions, one can isolate the four-vector $\mathcal{V}_\mu$ encoding the nucleon ground-state contribution to the matrix element of the electromagnetic current:

$$\mathcal{V}^\mu \equiv \frac{1}{4}\mathrm{Tr}[e^{i\alpha_N\gamma_5}\mathcal{P}_{3pt}e^{i\alpha_N\gamma_5}(-i\not{p}' + M_N)O^\mu(-i\not{p} + M_N)], \tag{25}$$

where O^μ is given in Eq. (23). The full expressions for $\mathcal{V}_{1,2,3,4}$, along with a general strategy for extracting F_3, from the four coupled complex equations is given in Appendix B.

TABLE II. The phase α_N for two values of the mass gap of the first excited state. In the first case, α_N is determined using $M_1 - M_0$ from a three-state fit to the real part of the two-point function. In the second, the $N(0)\pi(0)$ state is assumed to be the first excited state, in which case the mass gap in equal to M_π.

Ensemble	$M_1 - M_0$ [GeV]	α_N	M_π [GeV]	$\alpha_N^{N\pi}$
$a12m310$	0.54(18)	0.353(28)	0.3102(28)	0.375(29)
$a12m220$	0.67(13)	0.532(36)	0.2279(19)	0.597(46)
$a12m220L$	0.81(13)	0.590(43)	0.2276(17)	0.715(51)
$a09m310$	0.93(14)	0.243(16)	0.3130(28)	0.276(19)
$a09m220$	0.77(12)	0.321(39)	0.2259(18)	0.360(44)
$a09m130$	0.706(85)	0.551(43)	0.1381(10)	0.766(67)
$a06m135$	0.788(66)	0.393(64)	0.1356(14)	0.51(12)

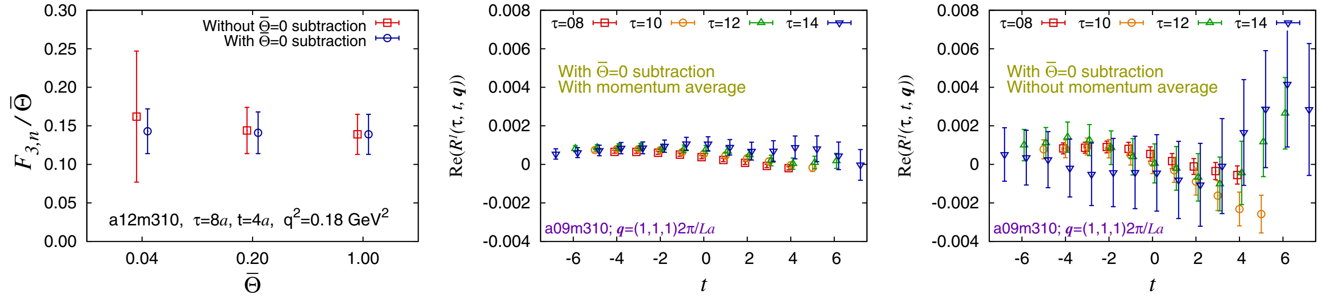

FIG. 12. The improvement in signal under subtraction of the $\bar{\Theta} = 0$ contribution and averaging over equivalent momenta. The panel on the left shows, using data from the $a12m310$ ensemble, (i) the improvement in $F_{3,n}$ as $\bar{\Theta} \to 0$ and (ii) even $\bar{\Theta} = 1$ is in the linear regime. The panel in the middle shows the signal in $R^1(\tau, t, \boldsymbol{q})$ with both the $\bar{\Theta} = 0$ subtraction and momentum averaging on the $a09m310$ ensemble with $\bar{\Theta} = 0.2$ and $\boldsymbol{q} = (1,1,1)2\pi/La$, while that on the right is without averaging over equivalent momenta.

To extract F_3, the $\not{C}\not{P}$ part of the three-point functions, a very significant simplification of the analysis and improvement in the signal is achieved by subtracting the $\bar{\Theta} = 0$ contribution from each component of the current in Eq. (25) before making the excited-state fits and decomposing the resulting ground-state matrix element in terms of form factors. This is implemented by analyzing the ground-state contribution in terms of the combination $\bar{\mathcal{V}}_\mu = \mathcal{V}_\mu(\bar{\Theta}) - \mathcal{V}_\mu(0)$. Working to first order in $\bar{\Theta}$, and recalling that $s_{\alpha_N} \equiv \sin\alpha_N \cos\alpha_N \sim \alpha_N \sim O(\bar{\Theta})$, and $F_3 \sim O(\bar{\Theta})$, the expressions for the ground-state contributions of the three-point functions $\bar{\mathcal{V}}_{1,2,3,4}$ in terms of form factors simplify to

$$\bar{\mathcal{V}}_1 = -\frac{1}{2} q_1 q_3 G_3, \tag{26a}$$

$$\bar{\mathcal{V}}_2 = -\frac{1}{2} q_2 q_3 G_3, \tag{26b}$$

$$\bar{\mathcal{V}}_3 = \frac{1}{2}(2M_N(E_N - M_N) s_{\alpha_N} G_1 - q_3^2 G_3), \tag{26c}$$

$$\begin{aligned}\bar{\mathcal{V}}_4 &= \frac{i}{2}(q_3(E_N + M_N)G_3 - 2q_3 M_N s_{\alpha_N} G_1),\\ &= i q_3 M_N\left(\frac{(E_N + M_N)}{2M_N} F_3 - s_{\alpha_N} G_E\right),\end{aligned} \tag{26d}$$

where $G_1 = F_1 + F_2$ and $G_3 = F_3 + s_{\alpha_N} F_2$. We solve the above system for G_1 and G_3. At $q^2 = 0$ there is a further simplification because $G_1(0) = Q_N + F_2(0)$, where Q_N is the nucleon charge. With this, we get

$$F_3(0) = G_3(0) - s_{\alpha_N}(G_1(0) - Q_N). \tag{27}$$

The largest contribution to G_3 comes from $s_{\alpha_N} F_2$, and the statistical error in the right-hand side is much smaller when $G_3(q^2) - s_{\alpha_N}(G_1(q^2) - Q_N)$ is extrapolated, rather than only $G_3(q^2)$ and combined with $s_{\alpha_N}\kappa_N$ using the precisely measured nucleon anomalous magnetic moment $G_1(0) - Q_N = F_2(0) \equiv \kappa_N$. Also, note that $G_3(q^2)$ can be obtained uniquely from $\bar{\mathcal{V}}_1$ and $\bar{\mathcal{V}}_2$ for a number of values of q^2, which provides a useful check. One can extend Eq. (27) to define

$$\tilde{F}_3(q^2) \equiv G_3(q^2) - s_{\alpha_N}(G_1(q^2) - Q_N) \tag{28}$$

as it improves the extraction of $F_3(0) = \tilde{F}_3(0)$ since the extrapolation of $\tilde{F}_3(q^2)$ to $q^2 \to 0$ shows better control.

The subtraction of the $\bar{\Theta} = 0$ contribution also allows averaging of the three-point functions over momenta related by cubic invariance, as seen by comparing the simpler Eqs. (26) with Eqs. (B8). We illustrate the improvement in the signal in Fig. 12. The averaging over equivalent cases (over momenta related by cubic symmetry and over $\bar{\mathcal{V}}_1$ and $\bar{\mathcal{V}}_2$) significantly reduces the statistical errors and improves the analysis of excited-state contamination (ESC) discussed next.

Previous work has suggested multiple ways of reducing the error in such calculations. A systematic study of various definitions of the topological charge was carried out in Ref. [62], and most definitions were seen to be highly correlated, with one outlier: a spectral projection method [63,64]. We have not investigated such fermionic definitions of the topological charge in this work. We did, however, study the proposals made in Refs. [43,44,65,66] to integrate the topological charge density in a limited volume about the nucleon three-point function to reduce the error. The motivation is the intuitive expectation based on cluster decomposition that the correlation between the two is short ranged; therefore, outside an appropriately selected volume, the topological density does not contribute to the signal but only to the noise. In Fig. 13 we show data for both $\alpha_N/\bar{\Theta}$ and $F_{3,n}/\bar{\Theta}$ with $G\tilde{G}(x)$ integrated over a 4D box of size $2 \times R_T$ in the time extent for the three ensembles at $a \approx 0.09$ fm. In the two heavier mass ensembles, $a09m310$ and $a09m220$, the results plateau for a R_T that is smaller than the time extent of the lattice, while the

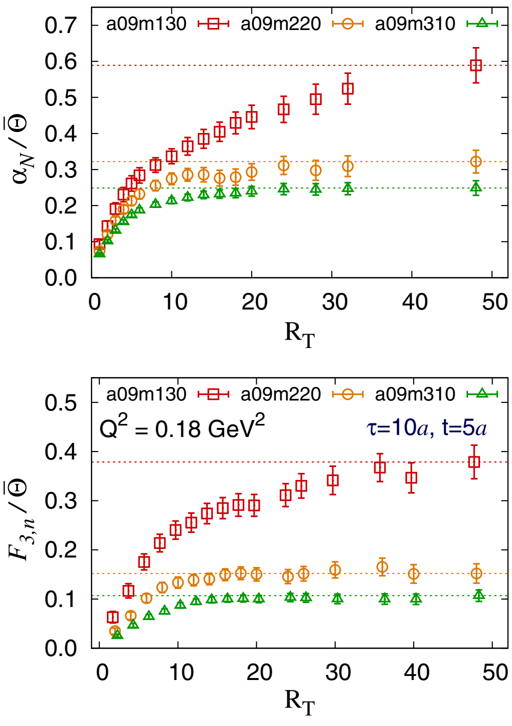

FIG. 13. The value of the phase α_N (upper) and $F_{3,n}$ form factor (lower) calculated using the topological charge density $G\tilde{G}(x)$ integrated over a 4D box with full extent in spatial directions and $2\times R_T$ in time about the neutron source $|t_Q - t_{\rm src}| \le R_T$ for α_N and from time slices $|t_Q - t_{\rm ins}| \le R_T$ about the current insertion for $F_{3,n}$. The dotted lines are the $R_T \to \infty$ estimates. These figures have already been presented in Ref. [67].

errors grow with R_T. In these cases, choosing the value with smaller errors near the start of the plateau would give an essentially unbiased estimate. This favorable situation, however, breaks down on our physical pion mass ensemble, $a09m130$. In this case there is no plateau, so we need to integrate over the full lattice or otherwise control for the extrapolation systematics to avoid using a biased value. Needless to say, even with integration over the full volume, there could be a bias on sufficiently small lattices but that is considered to be a part of the standard finite lattice size correction. Based on the size of the bias observed in Fig. 13 for $a09m130$, how slowly it goes to zero, and, more importantly, because we do not, *a priori*, know how to correct for such a bias, we do not use this variance reduction method on the current set of lattices. However, we do note, based on the data from the $a09m310$ and $a09m220$ ensembles, that for sufficiently large lattice volumes this method will become useful for even physical mass ensembles, but, even in those cases, one would need to estimate whether the gain due to error reduction is offset by the additional uncertainty arising from residual bias. The good news for this method is that such an analysis can be performed *a posteriori* and the appropriate R_T determined and used as long as the data for $\sum_x G\tilde{G}(x)$ are output by time slice, i.e., as a function of t with sums over only the spatial points. Alternately, the calculation of $\sum_x G\tilde{G}(x)$ over the appropriate region can be redone as it is inexpensive.

IX. REMOVING ESC IN F_3

In order to extract the ground-state contribution $\bar{\mathcal{V}}_\mu$ from lattice data on the ratio $R^\mu(\tau, t, \boldsymbol{q})$ of three- and two-point functions defined in Eq. (B7), we need to remove all excited states that make a significant contribution.

We have analyzed data on $R^\mu(\tau, t, \boldsymbol{q})$ in terms of a two-state fit, following two strategies. In the first, we have taken the first excited-state energies from a three-state fit to the two-point function. In the second strategy, we have set the first excited-state energy to the noninteracting energy of the $N\pi$ state, motivated by the χPT expectation that the leading excited state is the $N\pi$ state, with amplitude of the same size as the ground-state contribution (see Appendix D for more details). In Fig. 14 we compare the two strategies for $\mathrm{Im}(R^4(\tau, t, \boldsymbol{q}))$. The χ^2/d.o.f. of the fits are similar for the two cases on all three ensembles, but the ground-state estimate is vastly different and thus the contribution to the nEDM. With the current data, picking between them is the key unresolved challenge for this calculation. The very large extrapolation for $\tau \to \infty$ in the $N\pi$ case, however, leads us to question whether a two-state fit is sufficient if the $N\pi$ state is included and whether a similar effect might also contaminate our extraction of α_N. We therefore first perform the analysis taking the excited-state energy E_1 from a three-state fit to the two-point function and return to an analysis including a $N\pi$ state in Sec. XIII.

A second issue arising from the small signal in F_3 is that two-state fits to many of the correlation functions with the full covariance matrix are unstable with respect to variations in the values of τ and $t_{\rm skip}$, the number of points skipped in the fits adjacent to the source and sink for each τ. Examples of this are shown in Fig. 15 for $\mathrm{Re}(R^1(\tau, t, \boldsymbol{q}))$. This has two consequences for the analysis. First, we have carried out the final analysis using only the diagonal elements of the covariance matrix. We have, however, checked that in cases where fully covariant fits are possible, the two results are consistent. Since we use uncorrelated fits for removing excited-state contamination, we do not quote a χ^2/d.o.f. for these fits. Second, the system of four equations, Eqs. (26), overdetermines G_3 and G_1. While we solve the full set of equations as explained in Appendix B, the data from $\mathrm{Re}(R^{1,2}(\tau, t, \boldsymbol{q}))$, which have poor signal, do not make a significant contribution. We have checked this by removing them from the analysis and the results are essentially unchanged; i.e., the results are dominated by $\mathrm{Re}(R^3(\tau, t, \boldsymbol{q}))$ and $\mathrm{Im}(R^4(\tau, t, \boldsymbol{q}))$.

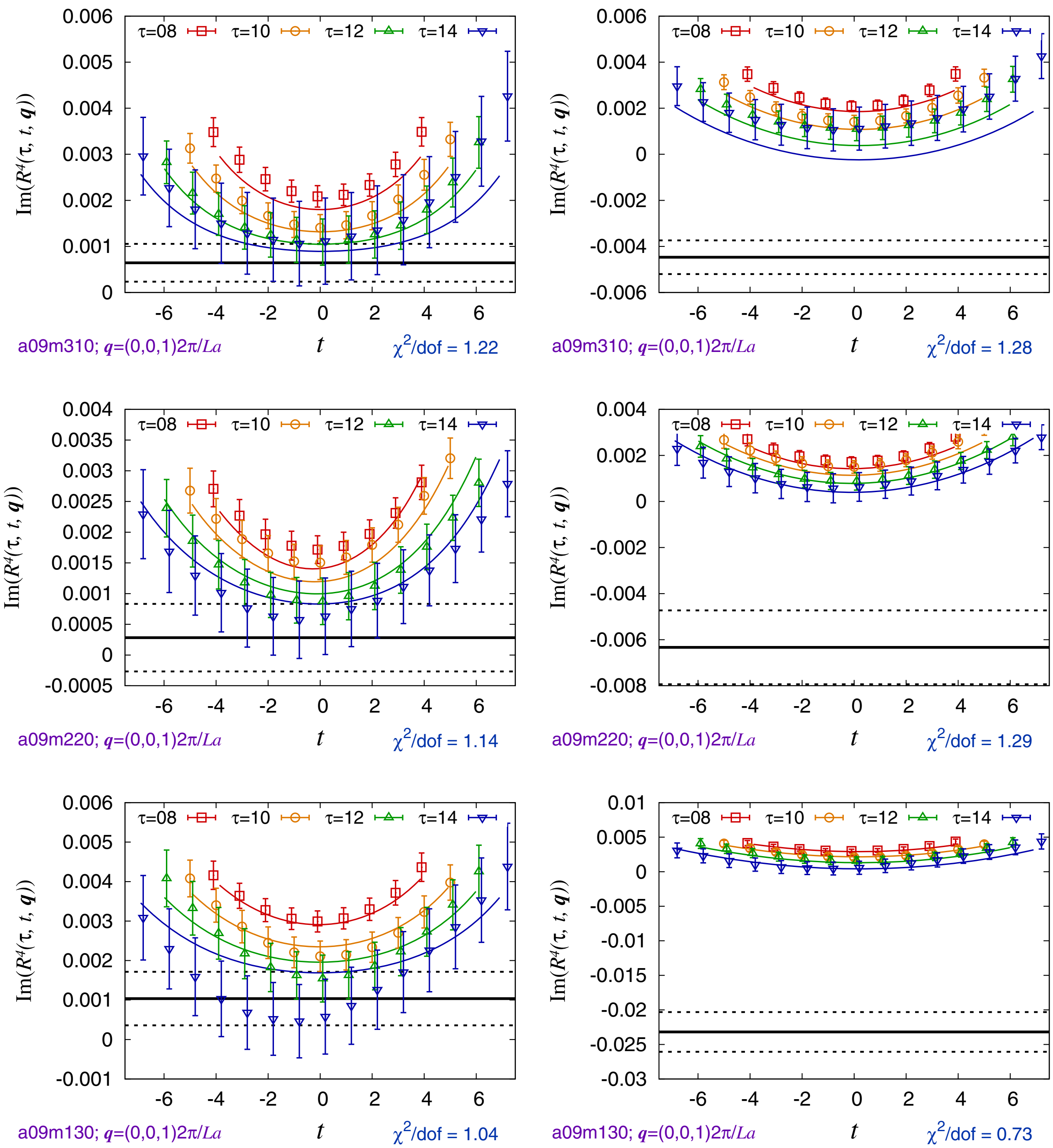

FIG. 14. Comparison of the two-state fit to the ratio $\mathrm{Im}(R^4(\tau, t, \boldsymbol{q}))$ defined in Eqs. (B7) with the first excited-state energies taken from a three-state fit to the two-point function (left panels) and set equal the noninteracting energy of the $N\pi$ state (right panels). The data for the three ensembles with $a \approx 0.09$ fm are shown in the three rows. The $\chi^2/\mathrm{d.o.f.}$ of the two sets of fits are comparable, but the extrapolated ground-state value (solid black line) is vastly different. The data are shown for $\boldsymbol{q} = (0, 0, 1)2\pi/La$ and the four largest values of τ. All data are with $\bar{\Theta} = 0.2$.

X. EXTRAPOLATION OF $F_3(q^2)$ TO $q^2 \to 0$

The ansatz used to extrapolate $F_3(q^2)$ to $q^2 \to 0$ is given in Eq. (C1) with one caveat. We use $\tilde{F}_3(q^2)$, defined in Eq. (28), instead of $F_3(q^2)$ as they are consistent to leading order and the extraction of $\tilde{F}_3(q^2)$ is better controlled. We examine three fits based on Eq. (C1).

(i) Linear: The quantities d_i and S'_i are free parameters and H_i is set to zero.

(ii) χPT: Only d_i is a free parameter, S'_i are given in Eq. (C11), $\bar{g}_0$ in Eq. (C7), and the H_i in Eq. (C13).

(iii) χPTg0: The same as χPT except $\bar{g}_0$ is left as a free parameter.

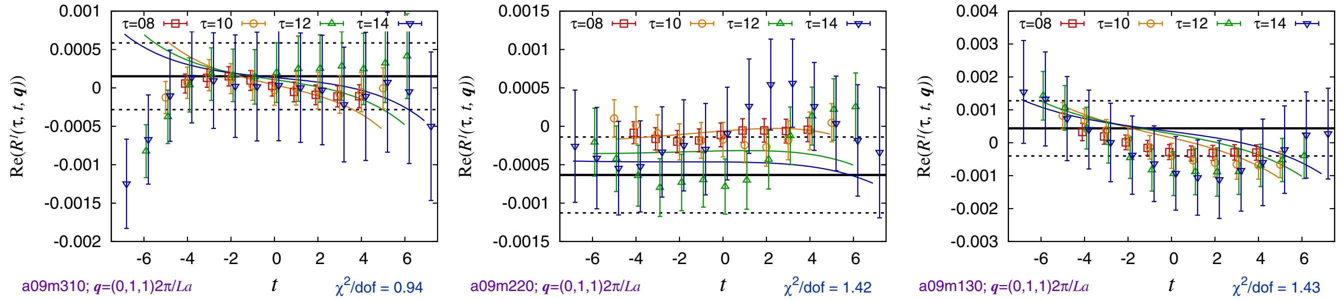

FIG. 15. Examples of unstable two-state fits to the ratio $\mathrm{Re}(R^1(\tau,t,\boldsymbol{q}))$ defined in Eqs. (B7) with the first excited-state energies taken from a three-state fit to the two-point function. The data are for the three ensembles with $a \approx 0.09$ fm, for $\boldsymbol{q} = (0,1,1)2\pi/La$ and the values of τ are specified in the labels. All data are with $\bar{\Theta} = 0.2$.

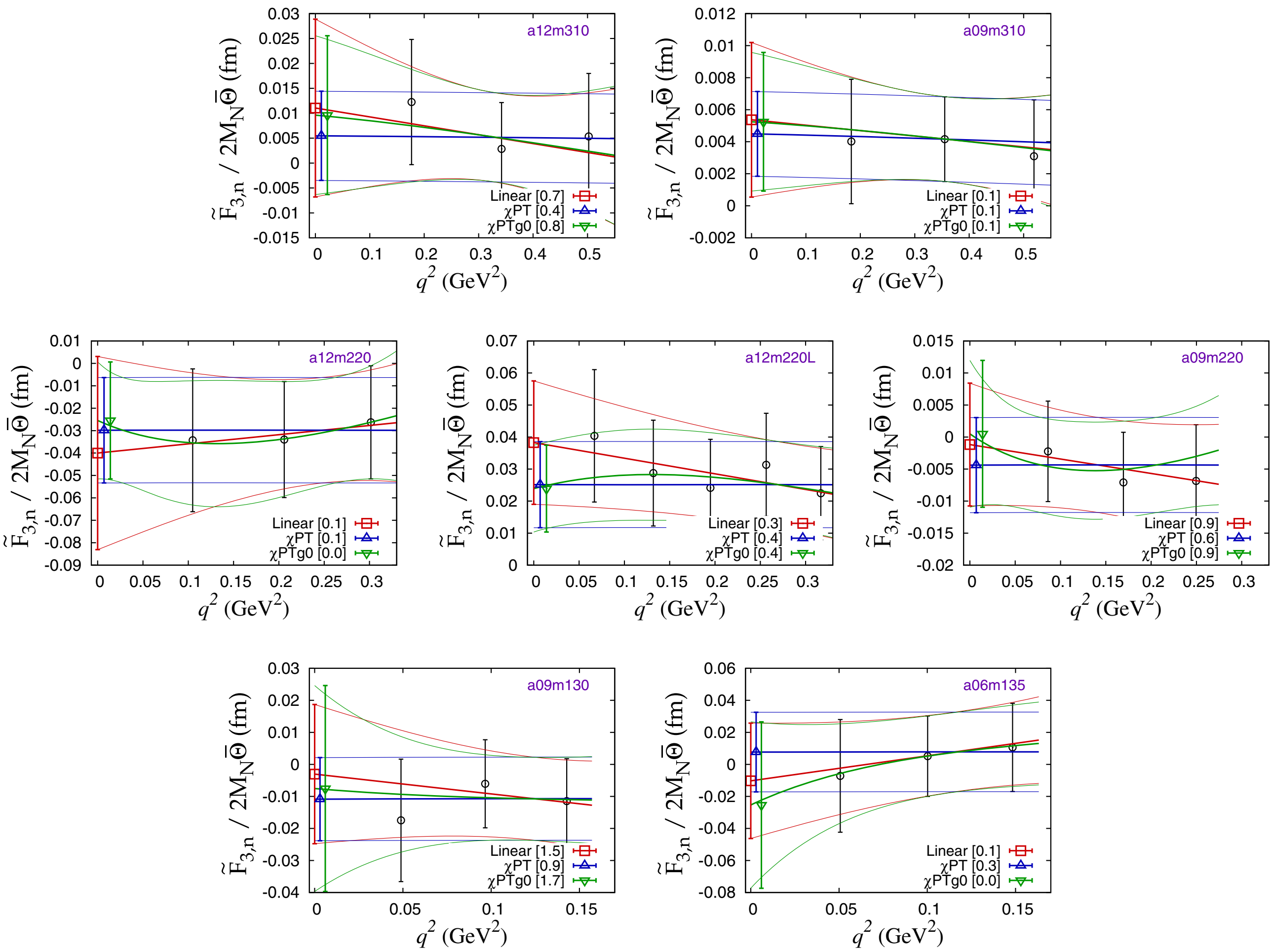

FIG. 16. The extrapolation of $\tilde{F}_3(q^2)$ to $q^2 \to 0$ using Eq. (C1) for the neutron. The three fit ansatz, linear, χPT and χPTg0, are defined in the text. The χ^2/d.o.f. of the fits are given within square brackets. All data are with $\bar{\Theta} = 0.2$.

The data and fits for the neutron and proton are presented in Figs. 16 and 17. The data are, within errors, flat in all cases and the extrapolated values from the three types of fits are consistent. Since in most cases, we have reliable data at only three values of q^2, we take the final result from the χPT fit. At the end, we will take the difference between the linear and χPT fits to estimate the associated systematic uncertainty.

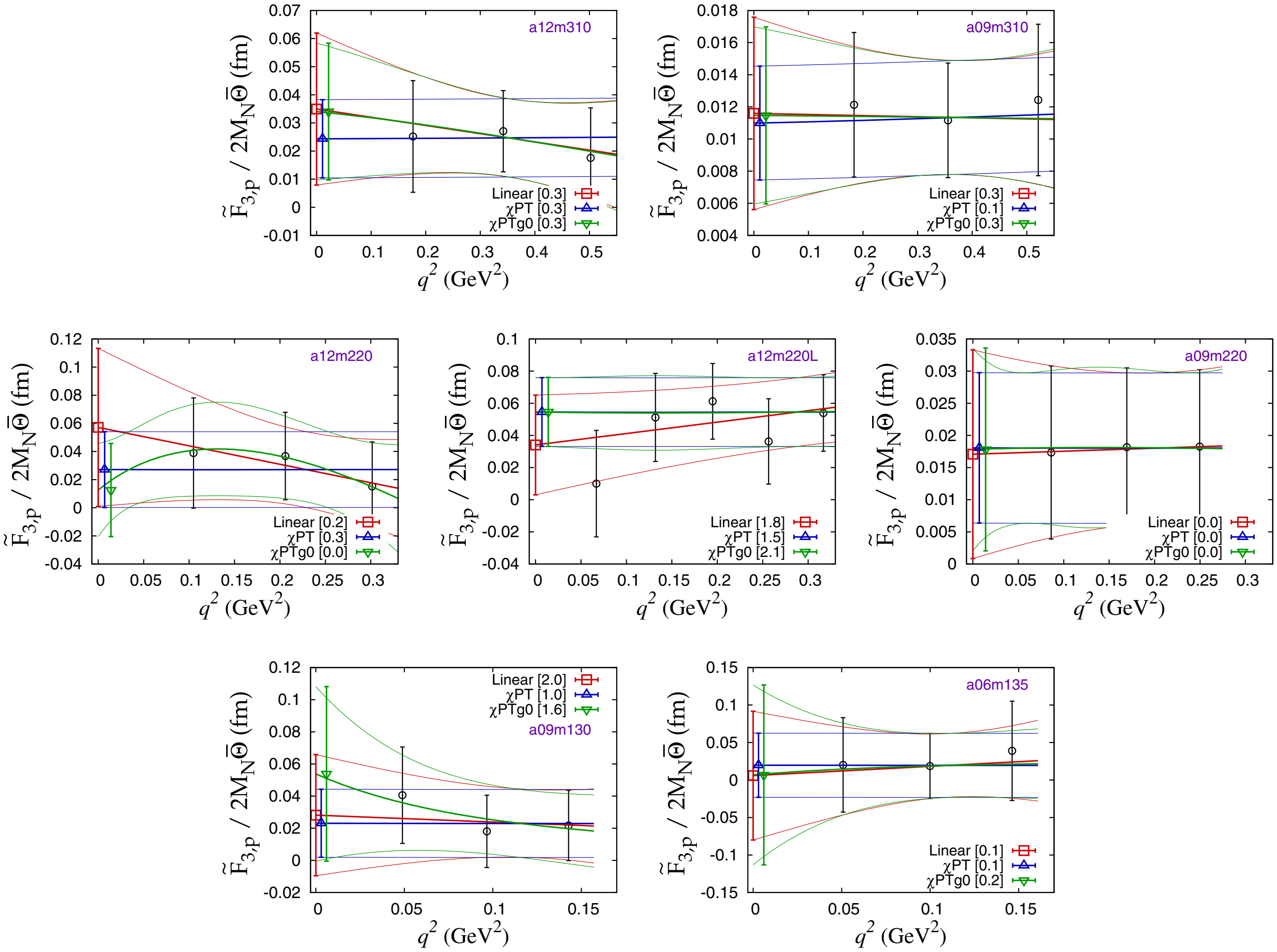

FIG. 17. The extrapolation of $\tilde{F}_3(q^2)$ to $q^2 \to 0$ using Eq. (C1) for the proton. The rest is the same as in Fig. 16.

XI. ADDITIONAL $O(a)$ ARTIFACTS

Before performing a chiral-continuum extrapolation of the results, in this section we justify our continuum extrapolation formula for $d_n(\bar{\Theta})$ that includes an M_π-independent term that does not vanish in the chiral limit, i.e., a term proportional to am_q^0.

There are multiple sources of $O(a)$ corrections that we need to consider. First, since our clover coefficient c_{SW} is set to its tadpole-improved tree-level value, the action, and hence all matrix elements, have residual $O(\alpha_s a)$ corrections. Because of the use of smeared gauge fields, however, the tadpole-improved tree-level approximation is extremely good, and these are expected to be tiny effects. Second, the vector current we insert is not improved [68], and, hence, we expect its renormalization coefficient to have $O(am_q)$ corrections. Such multiplicative terms, however, are unimportant near the chiral-continuum limit, where the $\cancel{CP}$ form factors vanish. A third source of $O(a)$ effects is the required improvement of the vector current by an $O(am_q^0)$ mixing with the derivative of the tensor current, which can give rise to a nonzero F_3, but only in the presence of CP violation in the theory. Since the topological charge does not introduce CP violation in the chiral limit, we would expect the behavior of d_n to be dominantly $O(a^2)$ in the chiral limit, if these were the only $O(a)$ effects.

In Appendix E, we analyze the Wilson-clover theory based on the framework of a continuum EFT for the lattice action and the axial Ward identities. Following Refs. [69–71], we show that the topological charge gives $O(a)$ $\cancel{CP}$ corrections and identify this as effectively due to the insertion of the isoscalar quark chromo-EDM operator, with which the topological term can mix. Since this term is expected to survive in the chiral limit, we include an $O(am_q^0)$ term in our chiral-continuum fits.

XII. CHIRAL-CONTINUUM EXTRAPOLATION AND RESULTS

In this section, we present the chiral-continuum (CC) extrapolation of data for d_n (and, similarly, d_p) obtained on the seven ensembles. For each, we examine four cases. These consist of two CC fits, linear and χPT, using the leading order terms

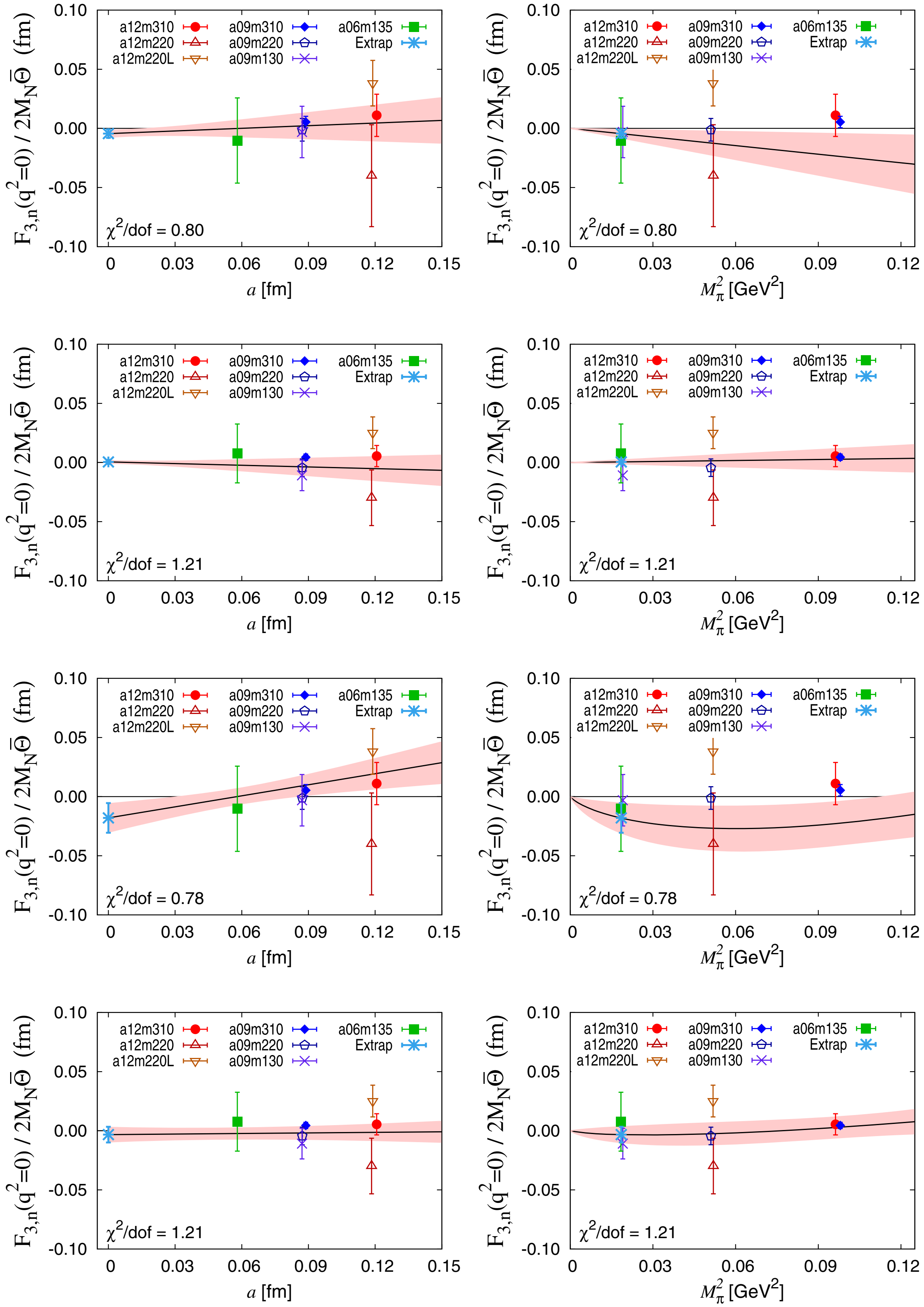

FIG. 18. The chiral-continuum extrapolation of d_n using the ansatz given in Eq. (30). The four rows show (i) a linear CC fit to the data obtained using a linear extrapolation in q^2 discussed in Sec. X; (ii) a linear CC fit to the data obtained using the χPT extrapolation in q^2; (iii) a χPT CC fit to the data obtained using a linear extrapolation in q^2; and (iv) a χPT CC fit to the data obtained using the χPT extrapolation in q^2. All data are with $\bar{\Theta} = 0.2$.

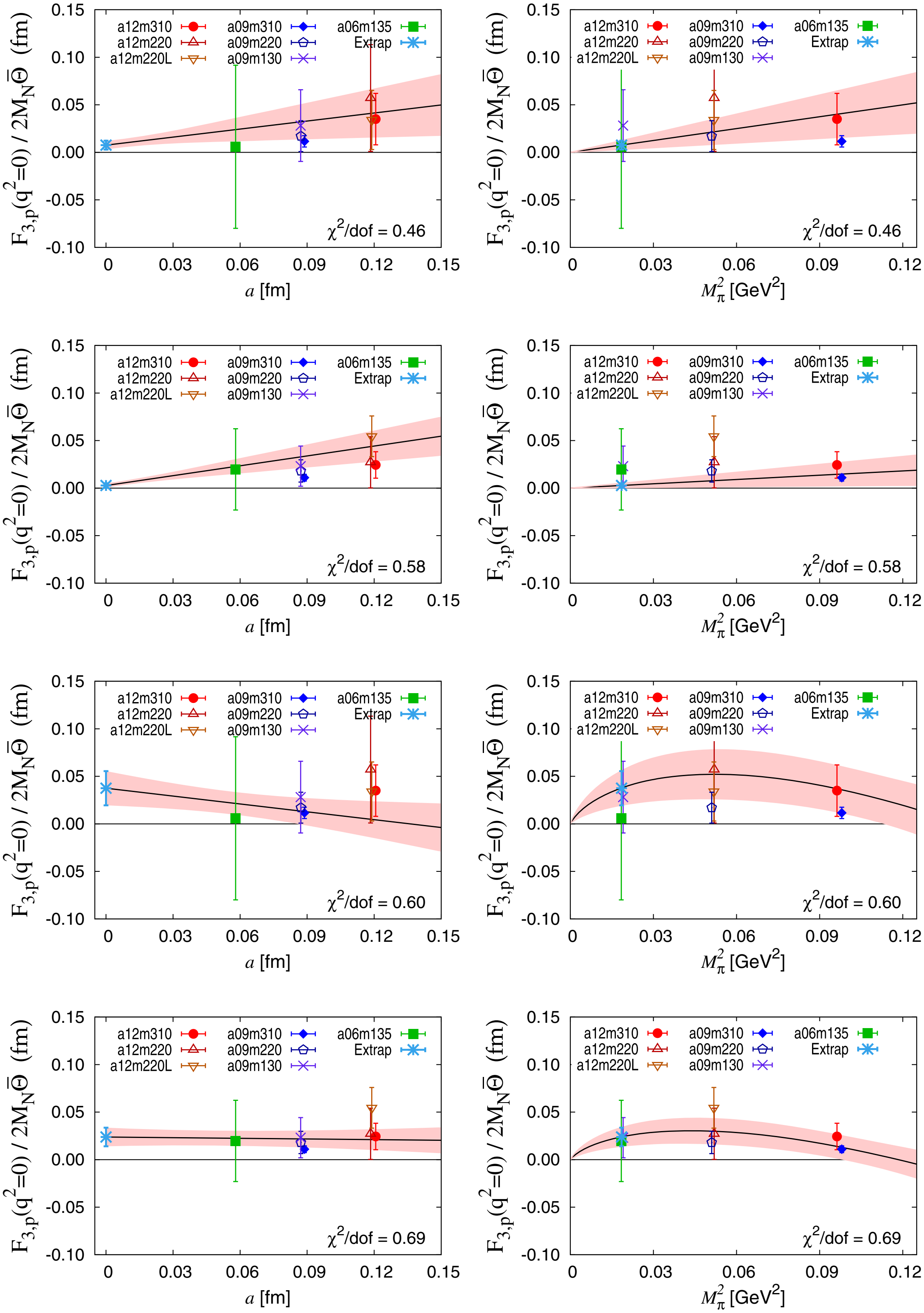

FIG. 19. The chiral-continuum extrapolation of d_p using the ansatz given in Eq. (30). The rest is the same as in Fig. 18.

TABLE III. Results for the contribution of the Θ-term to d_n and d_p for the four fit strategies defined in the text. Also given are the fit parameters c_i defined in Eqs. (29) and (30) and the χ^2/d.o.f. of the fit. Results are given for two choices of the first excited-state energy: (top) from a three-state fit to the two-point function and (bottom) the noninteracting $N\pi$ state.

Fit types	$F_3/2M_N$ [fm]	χ^2/d.o.f.	c_1 [fm-GeV^2]	c_2 [GeV^2]	c_{2L} [fm-GeV^2]	c_3
			Neutron			
Linear(q^2)|linear(CC)	−0.0044(36)	0.804	−0.24(20)	3.1(2.3)		0.02(16)
Linear(q^2)|χPT(CC)	−0.018(13)	0.782	0.76(62)		0.45(33)	0.31(18)
χPT(q^2)|linear(CC)	0.0005(17)	1.213	0.028(92)	0.8(1.2)		−0.06(11)
χPT(q^2)|χPT(CC)	−0.0032(66)	1.212	0.30(38)		0.12(19)	0.016(81)
			Proton			
Linear(q^2)|linear(CC)	0.0076(46)	0.455	0.42(25)	−7.6(3.4)		0.42(26)
Linear(q^2)|χPT(CC)	0.037(18)	0.597	−1.84(97)		−1.01(49)	−0.28(24)
χPT(q^2)|linear(CC)	0.0027(23)	0.578	0.15(13)	−4.8(1.9)		0.43(17)
χPT(q^2)|χPT(CC)	0.0238(98)	0.687	−1.40(58)		−0.70(28)	−0.02(11)
			Neutron (with $N\pi$ excited state)			
Linear(q^2)|linear(CC)	−0.0046(87)	1.402	−0.25(48)	10.6(7.8)		−0.79(70)
Linear(q^2)|χPT(CC)	−0.054(37)	1.323	3.2(2.2)		1.6(1.1)	0.27(45)
χPT(q^2)|linear(CC)	0.0039(42)	2.246	0.22(23)	8.4(3.8)		−1.07(37)
χPT(q^2)|χPT(CC)	−0.028(18)	2.430	2.5(1.1)		1.04(52)	−0.26(20)
			Proton (with $N\pi$ excited state)			
Linear(q^2)|linear(CC)	0.019(12)	0.347	1.04(66)	−29(12)		2.2(1.0)
Linear(q^2)|χPT(CC)	0.140(54)	0.358	−7.7(3.2)		−4.0(1.6)	−0.70(66)
χPT(q^2)|linear(CC)	0.0040(50)	0.398	0.22(27)	−15.7(5.4)		1.51(52)
χPT(q^2)|χPT(CC)	0.068(25)	0.522	−4.4(1.6)		−2.09(75)	−0.02(27)

$$d_n(a, M_\pi) = c_1 M_\pi^2 + c_2 a M_\pi^2 + c_3 a, \tag{29}$$

$$d_n(a, M_\pi) = c_1 M_\pi^2 + c_{2L} M_\pi^2 \ln\left(\frac{M_\pi^2}{M_N^2}\right) + c_3 a, \tag{30}$$

where the term $c_3 a$ is the $O(a)$ effect discussed in Sec. XI, because of which $d_{n,p}$ do not vanish in the chiral limit at finite a. The ansatz are distinguished by the terms proportional to c_2 (linear) and c_{2L} (χPT). In these fits, M_N is set to its physical value 940 MeV. We make these two fits to the data for $d_{n,p}$ obtained using (i) the linear and (ii) χPT extrapolation in q^2, which leads to four estimates. These four CC fits for the neutron and the proton are shown in Figs. 18 and 19. The results and the fit coefficients c_i are given in Table III.

As discussed in Appendix C, at next-to-leading order (NLO) in χPT the coefficient of the chiral logarithm c_{2L} is fixed in terms of the isovector scalar charge, the quark condensate and the pion decay constant, leading to $(c_{2L})_n = -(c_{2L})_p = 0.033$ fm-GeV^2. Although the central values from the fits are approximately one order of magnitude larger, our results are compatible with this estimate at the 1σ–2σ level.

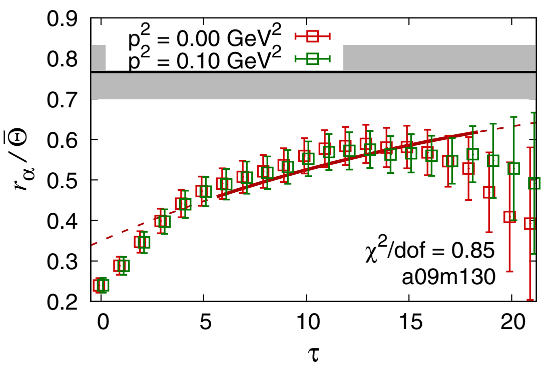

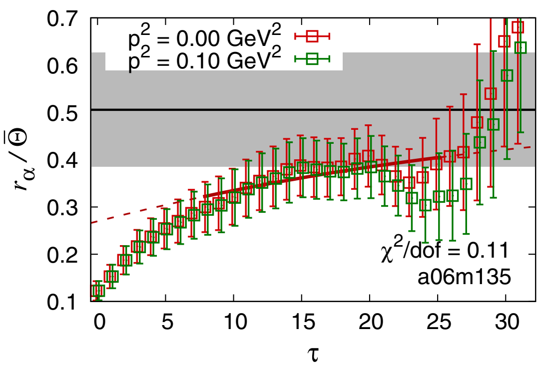

FIG. 20. The increase in the value of α when fits to the two-point functions are made including a $N\pi$ excited state as compared to data in Fig. 11.

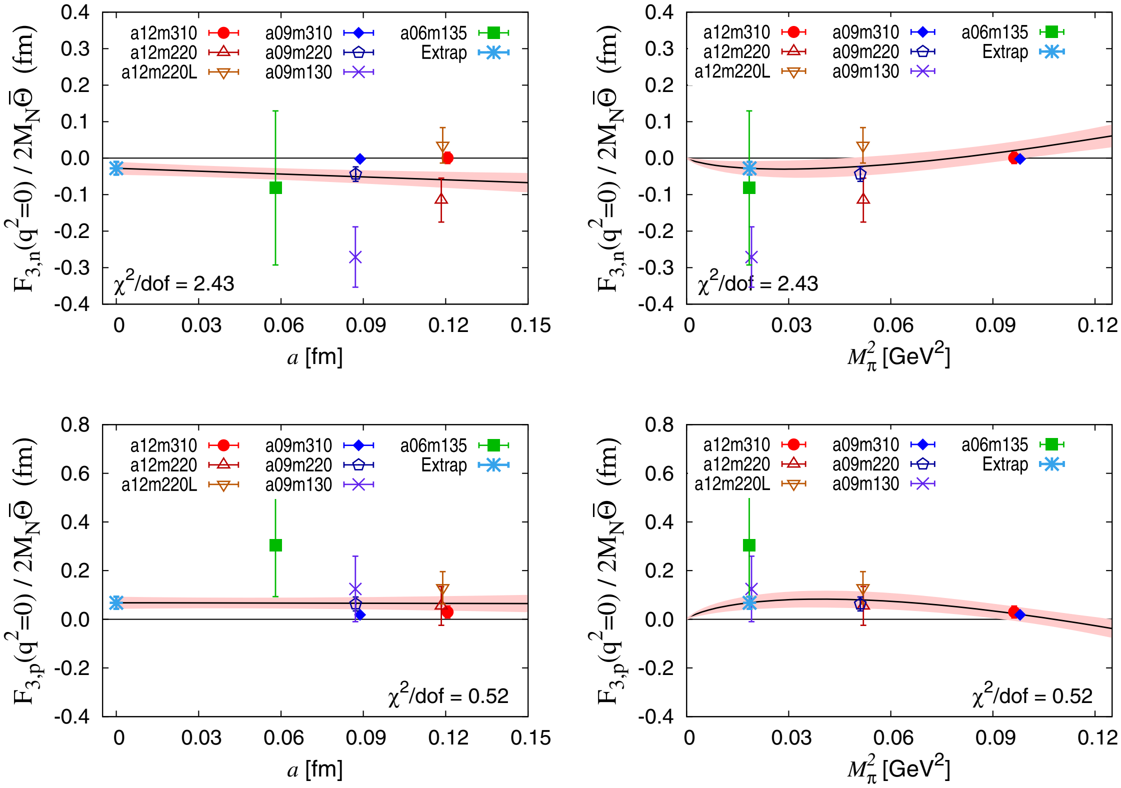

FIG. 21. The chiral-continuum extrapolation of d_n (top) and d_p (bottom) using the ansatz given in Eq. (30), using $N\pi$ as the excited-state fits, and with the $\chi\mathrm{PT}(q^2)|\chi\mathrm{PT}(\mathrm{CC})$ strategy. All data are with $\bar{\Theta} = 0.2$.

For the final central values for $d_{n,p}$ defined in Eq. (4), we take the $\chi\mathrm{PT}(q^2)|\chi\mathrm{PT}(\mathrm{CC})$ results

$$d_n = -0.003(7)(20)\bar{\Theta}\ e\cdot\mathrm{fm}, \qquad (31)$$

$$d_p = 0.024(10)(30)\bar{\Theta}\ e\cdot\mathrm{fm}, \qquad (32)$$

where the second systematic error is the spread in the four estimates given in Table III.

XIII. ANALYSIS INCLUDING THE $N\pi$ EXCITED STATE

In this section, we describe how all ground-state quantities change when the $N\pi$ excited state is included. This analysis should be considered exploratory because (i) the extrapolations in the fits to remove ESC (see Fig. 14), (ii) the errors, and (iii) the cancellations when combining different terms to get F_3 using Eqs. (26) are all large.

In Fig. 20, we show the increase in the value of α for the two physical mass ensembles as compared to the data presented in Fig. 11. The q^2 behavior is similar to that shown in Figs. 16 and 17, and the final results for the four strategies are given in Table III. The CC fits for the neutron and the proton using the $\chi\mathrm{PT}(q^2)|\chi\mathrm{PT}(\mathrm{CC})$ strategy are shown in Fig. 21.

For the central value we again take the $\chi\mathrm{PT}(q^2)|\chi\mathrm{PT}(\mathrm{CC})$ results

$$d_n|_{N\pi} = -0.028(18)(54)\bar{\Theta}\ e\cdot\mathrm{fm}, \qquad (33)$$

$$d_p|_{N\pi} = 0.068(25)(120)\bar{\Theta}\ e\cdot\mathrm{fm}, \qquad (34)$$

where the second systematic error is the spread in the four estimates given in Table III.

XIV. COMPARISON TO PREVIOUS WORK

There are two estimates [44,72] of the contribution of the Θ-term to the nEDM since the clarification of the impact of the phase α that arises in the nucleon spinor in a theory with $\not{C}\not{P}$ in Ref. [47]. That work also contains a review of previous results, which after correction were consistent with zero. No estimate is given in Ref. [47], but there is a preliminary value in a subsequent conference proceedings, Ref. [66]. All three post-Ref. [47] calculations use the small Θ expansion and gradient flow method for topological charge renormalization as employed in this work. All these results are summarized in Table IV.

The ETM Collaboration [72] has performed the calculation on one $2+1+1$-flavor twisted mass clover-improved ensemble with $a = 0.0801(4)$ fm, $M_\pi = 139(1)$ MeV, and $M_\pi L = 3.62$. Data are presented for a single value of $\tau = 12$

TABLE IV. Summary of lattice results for the contribution of the Θ-term to the neutron and proton electric dipole moment.

	Neutron [$\bar{\Theta}$ e · fm]	Proton [$\bar{\Theta}$ e · fm]
This work	$d_n = -0.003(7)(20)$	$d_p = 0.024(10)(30)$
This work with $N\pi$	$d_n = -0.028(18)(54)$	$d_p = 0.068(25)(120)$
ETMC [72]	$\lvert d_n\rvert = 0.0009(24)$	
Dragos *et al.* [44]	$d_n = -0.00152(71)$	$d_p = 0.0011(10)$
Syritsyn *et al.* [66]	$d_n \approx 0.001$	

so there is no information on excited-state effects, continuum extrapolation, chiral behavior, or finite-size effects. They also implicitly implement the $\bar{\Theta} = 0$ subtraction [see Eqs. (26)] that we find reduces the statistical noise by using the spin projector $(1+\gamma_4)i\gamma_5\gamma_k/4$. They determine $F_3(0)$ by making a constant fit to the lowest three q^2 points. Their final result is taken using the spectral projectors method, which they find reduces the errors by a factor of about 2 compared to the field-theoretic definition of the topological charge used in this work. They do not assess a systematic error associated with excited-state effects or extrapolation in q^2 or to the continuum limit.

The calculation presented in Ref. [44] uses six 2 + 1-flavor Wilson-clover ensembles but only one below $M_\pi = 567$ MeV, with $M_\pi = 410$ MeV. The values of lattice spacings range between $0.068 < a < 0.11$ fm. A linear fit in q^2 is made to obtain $F_3(0)$. Also, artifacts due to ESC are not analyzed and, in any case, their data with the heavy pion masses studied, $M_\pi > 410$ MeV, would not be sensitive to analyses with or without including a $N\pi$ state. This is the only other calculation that has presented a chiral extrapolation using the χPT ansatz [Eq. (30) but with a $O(a^2)$ discretization correction instead of our $c_3 a$ term]. As shown in the bottom right panels in Figs. 18 and 19, such chiral fits have an inflection point close to the smallest M_π data point in order to satisfy the constraint $F_3 = 0$ at $M_\pi = 0$. In the case of Ref. [44], this occurs around $M_\pi = 400$ MeV, raising questions on the reliability of the extrapolation.

XV. CONCLUSIONS

This paper presents a calculation of the contribution of the Θ-term to the nucleon electric dipole moment using 2 + 1 + 1-flavor HISQ ensembles and Wilson-clover valence quarks. Two of the seven ensembles analyzed are at the physical pion mass, which anchor our chiral fits. The calculation has been done using the small Θ expansion method. Significant effort has been devoted to getting a reliable signal in the $\not{C}\not{P}$ violating form factor F_3. The gradient flow scheme has been used to renormalize the Θ-term and the results are shown to be independent of the flow time. Our estimate of the topological susceptibility for the 2 + 1 + 1 theory is $\chi_Q = (66(9)(4)\ \mathrm{MeV})^4$ in the continuum limit at $M_\pi = 135$ MeV.

We also present two technical issues. First, in Appendix D, we show that, in chiral perturbation theory, the $N\pi$ excited state should provide the dominant contamination. We have, therefore, used two strategies for removing excited-state contamination. In the first, the mass gaps are taken from fits to the spectral decomposition of the nucleon two-point function, and in the second we assume they are given by the noninteracting energy of the $N(\mathbf{0})\pi(\mathbf{0})$ state. We find a very significant difference between the two as shown in Secs. IX and XIII and by the results summarized in Tables III and IV.

The second technical issue discussed in Sec. XI and Appendix E is that, for Wilson-type fermions, lattice artifacts introduce a term proportional to am_q^0, because of which d_n does not vanish in the chiral limit at finite a. Our chiral-continuum fits have been made including this term.

The analysis of the q^2 dependence of F_3^Θ has been carried out using both a linear and the leading order χPT expression as described in Sec. X. The current data do not distinguish between the two. Similarly, fits versus M_π^2 are also carried out using a linear and the leading order χPT expression as described in Sec. XII. The results from these four sets of fits and the two strategies to remove excited-state contributions are summarized in Table III.

Our preferred values are obtained using the leading order χPT expressions. The analysis using excited states from fits to the two-point function indicate that d_n^Θ is small, $|d_n^\Theta| \lesssim 0.01\bar{\Theta}$ e · fm, whereas for the proton we get $|d_p^\Theta| \sim 0.02\bar{\Theta}$ e · fm. On the other hand, if the dominant excited-state contribution is from the $N\pi$ state, then $|d_n^\Theta|$ could be as large as $0.05\bar{\Theta}$ e · fm and $|d_p^\Theta| \sim 0.07\bar{\Theta}$ e · fm. Lastly, we find the sign of d_p^Θ to be opposite to that of d_n^Θ.

From the final summary of results presented in Table IV, which also includes estimates from previous works, it is clear that, at present, lattice calculations do not provide a reliable estimate. To improve the current 100% uncertainty to a 3σ result will require a factor of at least 10 improvement in statistics.

ACKNOWLEDGMENTS

The calculations used the Chroma software suite [73]. This research used resources at (i) the National Energy Research Scientific Computing Center, a Department of Energy (DOE) Office of Science User Facility supported by the Office of Science of the U.S. Department of Energy under Contract No. DE-AC02-05CH11231; (ii) the Oak Ridge Leadership Computing Facility, which is a DOE Office of Science User Facility supported under Contract No. DE-AC05-00OR22725; (iii) the USQCD

Collaboration, which are funded by the Office of Science of the U.S. Department of Energy, and (iv) Institutional Computing at Los Alamos National Laboratory. The work was supported by the U.S. Department of Energy, Office of Science, Office of High Energy Physics and Office of Nuclear Physics through the Los Alamos National Laboratory, which is operated by Triad National Security, LLC, for the National Nuclear Security Administration of U.S. Department of Energy under Contract No. 89233218CNA000001. We acknowledge support from the U.S. Department of Energy, Office of Science, Office of Advanced Scientific Computing Research and Office of Nuclear Physics, Scientific Discovery through Advanced Computing (SciDAC) program, and of the U.S. Department of Energy Exascale Computing Project. T. B., V. C., R. G., E. M. and B. Y. were partly supported by the LANL LDRD program.

APPENDIX A: CONNECTION BETWEEN MINKOWSKI AND EUCLIDEAN NOTATIONS

To make our conventions explicit, we present the connection between Minkowski and Euclidean variables in Table V.

To connect the Lagrangian density for the Θ term in Minkowski and Euclidean spaces, we take the Minkowski action associated with the QCD Θ-term to be

$$S_\Theta^M = -\frac{\Theta}{32\pi^2}\int d^4x (G_M)^{a\mu\nu}(x)(\tilde{G}_M)^a_{\mu\nu}(x), \quad \text{(A1)}$$

where $(\tilde{G}_M)^a_{\mu\nu} = (1/2)\epsilon_M^{\mu\nu\alpha\beta}(G_M)^a_{\alpha\beta}$ and $(\epsilon_M)_{0123} = +1 = -\epsilon_M^{0123}$. Upon rotating to the Euclidean space one gets $d^4x_M = -id^4x_E$ and

$$\epsilon_M^{\mu\nu\alpha\beta}(G_M)^a_{\mu\nu}(G_M)^a_{\alpha\beta} = i(\epsilon_E)_{\mu\nu\alpha\beta}(G_E)^a_{\mu\nu}(G_E)^a_{\alpha\beta}. \quad \text{(A2)}$$

The factor of $+i$ arises from the transformation of the field strength and because each term in the sum has one factor of G_{0i} (or G_{i0}) and one factor of G_{jk}. Moreover, we used

$$\epsilon_M^{0ijk} \equiv (\epsilon_E)_{4ijk} = (\epsilon_E)^{4ijk}, \quad \text{(A3)}$$

which implies

$$(\epsilon_E)_{ijk4} = -(\epsilon_M)^{0ijk} \quad \text{(A4)}$$

and hence $(\epsilon_E)_{1234} = +1$.

Making these changes in the Lagrangian density and the measure in the right-hand side of Eq. (A1) gives

$$S_\Theta^M = -\frac{\Theta}{64\pi^2}\epsilon_E^{\mu\nu\alpha\beta}\int d^4x_E (G_E)^a_{\mu\nu}(x)(G_E)^a_{\alpha\beta}(x), \quad \text{(A5)}$$

and hence $(iS^M = -S^E)$

$$S_\Theta^E = +i\frac{\Theta}{64\pi^2}\epsilon_E^{\mu\nu\alpha\beta}\int d^4x_E (G_E)^a_{\mu\nu}(x)(G_E)^a_{\alpha\beta}(x), \quad \text{(A6)}$$

consistently with Eq. (1).

TABLE V. Connection between Euclidean and Minkowski variables.

Quantity	Minkowski ↔ Euclidean	Remarks
4-vector v^μ	$v_M^0 = v_{M0} = -iv_E^4 = -iv_{E4}$ $v_M^i = -v_{Mi} = v_E^i = v_{Ei}$ $t \equiv x_M^0 = -ix_E^4 \equiv -i\tau$ $p_M^0 = -ip_E^4 = E$	Ensures $v_M \cdot v_M' = -v_E \cdot v_E'$; in particular, $v_M^2 = -v_E^2$.
Derivatives	$\partial_0^M = i\partial_4^E$ $\partial^{Mi} = -\partial_i^M = -\partial_i^E = -\partial^{Ei}$	$\partial_\mu = \partial/\partial x^\mu$ and $\partial^\mu = \partial/\partial x_\mu$ in both E and M
Gauge fields	$A_0^M = iA_4^E$ $A^{Mi} = -A_i^M = -A_i^E = -A^{Ei}$ $(G_M)^{0i} = -i(G_E)^{4i}$, $(G_M)_{0i} = i(G_E)_{4i}$ $(G_M)^{ij} = (G_E)^{ij}$, $(G_M)_{ij} = (G_E)_{ij}$	$D_\mu = \partial_\mu - A_\mu$ transforms homogeneously
γ matrices	$\gamma_E^4 = \gamma_M^0$, $\gamma_E^i = -i\gamma_M^i$ $\gamma_E^5 = \gamma_E^1\gamma_E^2\gamma_E^3\gamma_E^4 = -i\gamma_M^0\gamma_M^1\gamma_M^2\gamma_M^3 = -\gamma_M^5 = -\gamma_c^5$ $\gamma_M^\mu \equiv \gamma_{c1}\gamma_{c3}\gamma_c^\mu\gamma_c^3\gamma_c^1$ $\not{p}_M = -i\not{p}_E$ $\not{D}_M = i\not{D}_E$	We adopt the DeGrand-Rossi basis [74]. These Euclidean gamma matrices are Hermitian. Minkowski gamma matrices are unitarily transformed from the standard chiral basis γ_c^μ [75]. $\psi_M = \gamma_{c1}\gamma_{c3}\psi_c$ and $\bar{\psi}_M = \bar{\psi}_c\gamma_c^3\gamma_c^1$.
Charge Conjugation Matrix	$C_M = i\gamma_0^M\gamma_2^M$ $C_c = i\gamma_0^c\gamma_2^c$ $C_E = \gamma_2^E\gamma_4^E$	

APPENDIX B: EXTRACTION OF F_3

The Euclidean four-vector $\mathcal{V}^\mu(\mathbf{q})$ defined in Eq. (25) can be determined from lattice data by taking appropriate ratios of three-point function and two-point functions. This is achieved by defining the projected two- and three-point functions as follows:

$$\mathcal{C}_{\mathrm{2pt}}(t,\boldsymbol{p}) = \mathrm{Tr}[\mathcal{P}_{\mathrm{2pt}}\langle\Omega|N(\boldsymbol{p},t)\bar{N}(\boldsymbol{p},0)|\Omega\rangle], \quad \text{(B1)}$$

$$\mathcal{C}^\mu_{\mathrm{3pt}}(\tau,t,\boldsymbol{q}) = \mathrm{Tr}[\mathcal{P}_{\mathrm{3pt}}\langle\Omega|N(\boldsymbol{p}',\tau)J^{\mathrm{EM}\mu}(t)\bar{N}(\boldsymbol{p},0)|\Omega\rangle], \quad \text{(B2)}$$

with $\boldsymbol{q}=\boldsymbol{p}'-\boldsymbol{p}$, $\boldsymbol{p}'=0$, $\mathcal{P}_{\mathrm{3pt}}$ given in Eq. (24),

$$\mathcal{P}_{\mathrm{2pt}} = \frac{1}{2}(1+\gamma_4), \quad \text{(B3)}$$

and, neglecting the contributions of heavier quarks,

$$J^{\mathrm{EM}}_\mu = e((2/3)\bar{u}\gamma_\mu u - (1/3)\bar{d}\gamma_\mu d - (1/3)\bar{s}\gamma_\mu s). \quad \text{(B4)}$$

The ratio

$$\tilde{R}^\mu \equiv \frac{\mathcal{C}^\mu_{\mathrm{3pt}}(\tau,t,\boldsymbol{q})}{\mathcal{C}_{\mathrm{2pt}}(\tau,\boldsymbol{p}')} \times \left(\frac{\mathcal{C}_{\mathrm{2pt}}(t,\boldsymbol{p}')\mathcal{C}_{\mathrm{2pt}}(\tau,\boldsymbol{p}')\mathcal{C}_{\mathrm{2pt}}(\tau-t,\boldsymbol{p})}{\mathcal{C}_{\mathrm{2pt}}(t,\boldsymbol{p})\mathcal{C}_{\mathrm{2pt}}(\tau,\boldsymbol{p})\mathcal{C}_{\mathrm{2pt}}(\tau-t,\boldsymbol{p}')}\right)^{1/2} \quad \text{(B5)}$$

becomes independent of t and τ when t and τ are sufficiently large that excited-state effects can be neglected and takes the form

$$\frac{\mathcal{V}^\mu(\boldsymbol{q})}{\sqrt{E_p E_{p'}(E_p+M_N\cos(2\alpha_N))(E_{p'}+M_N\cos(2\alpha_N))}}. \quad \text{(B6)}$$

In our plots to demonstrate the signal and the contribution of excited states, we choose to show the quantity

$$R^\mu(\tau,t,\boldsymbol{q}) \equiv \frac{\tilde{R}^\mu}{g_V}\sqrt{E_p E_{p'}(E_p+M_N\cos(2\alpha_N))(E_{p'}+M_N\cos(2\alpha_N))}, \quad \text{(B7)}$$

where $g_V \equiv \mathcal{C}^\mu_{\mathrm{3pt}}(\tau,t,\mathbf{0})/\mathcal{C}_{\mathrm{2pt}}(t,\mathbf{0})$ and α_N is calculated from fits to the two-point functions with momentum p or p' as discussed in Sec. VII.

The components of $\mathcal{V}_\mu$ are expressed in terms of form factors $F_{1,2,3,A}(q^2)$ defined in Eq. (6) as follows:

$$\begin{aligned}\mathcal{V}_1 &= ic_{\alpha_N}M_N(q_2+iq_1)F_1(q^2) + \left\{-c_{\alpha_N}M_N q_2 - \frac{1}{2}[s_{\alpha_N}q_1q_3 + ic_{\alpha_N}q_1(E_N-M_N)]\right\}F_2(q^2)\\ &\quad - 2i[s_{\alpha_N}q_2(E_N-m_N) - c_{\alpha_N}q_1q_3]F_A(q^2) - \frac{1}{2}[c_{\alpha_N}q_1q_3 - is_{\alpha_N}q_1(E_N-M_N)]F_3(q^2),\end{aligned} \quad \text{(B8a)}$$

$$\begin{aligned}\mathcal{V}_2 &= c_{\alpha_N}M_N(q_1+iq_2)F_1(q^2) + \left\{c_{\alpha_N}M_N q_1 - \frac{1}{2}[s_{\alpha_N}q_2q_3 + ic_{\alpha_N}q_2(E_N-M_N)]\right\}F_2(q^2)\\ &\quad + 2i[s_{\alpha_N}q_1(E_N-m_N) + c_{\alpha_N}q_2q_3]F_A(q^2) - \frac{1}{2}[c_{\alpha_N}q_2q_3 - is_{\alpha_N}q_2(E_N-M_N)]F_3(q^2),\end{aligned} \quad \text{(B8b)}$$

$$\begin{aligned}\mathcal{V}_3 &= M_N[ic_{\alpha_N}q_3 + s_{\alpha_N}(E_N-M_N)]F_1(q^2) + \frac{1}{2}\{-ic_{\alpha_N}(E_N-M_N)q_3 - s_{\alpha_N}q_3^2 + 2s_{\alpha_N}M_N(E_N-M_N)]\}F_2(q^2)\\ &\quad - 2ic_{\alpha_N}[q_1^2+q_2^2]F_A(q^2) - \frac{1}{2}[c_{\alpha_N}q_3^2 - is_{\alpha_N}q_3(E_N-M_N)]F_3(q^2),\end{aligned} \quad \text{(B8c)}$$

$$\begin{aligned}\mathcal{V}_4 &= M_N[c_{\alpha_N}(E_N+M_N) - is_{\alpha_N}q_3]F_1(q^2) - \frac{1}{2}\{c_{\alpha_N}(E_N^2-M_N^2) - is_{\alpha_N}q_3(E_N-M_N)]\}F_2(q^2)\\ &\quad + \frac{1}{2}[ic_{\alpha_N}q_3(E_N+M_N) + s_{\alpha_N}(E_N^2-M_N^2)]F_3(q^2),\end{aligned} \quad \text{(B8d)}$$

where $c_\alpha \equiv (\cos 2\mathrm{Re}\alpha + \cosh 2\mathrm{Im}\alpha)/2$ and $s_\alpha \equiv (\sin 2\mathrm{Re}\alpha + i\sinh 2\mathrm{Im}\alpha)/2$. For PT symmetric theories, where α is real, these expressions simplify to $c_\alpha = \cos^2\alpha$ and $s_\alpha = \cos\alpha\sin\alpha$.

From the above expressions we want to extract $F_3(q^2)$, which gives the neutron EDM. It turns out that the rhs of Eqs. (B8) is most naturally expressed in terms of $G_{1,2,3}$ given by

$$G_1 = F_1 + F_2, \tag{B9a}$$

$$G_2 = F_1 - \frac{q_E^2}{4m^2}F_2 + \frac{s}{c}\frac{q_E^2}{4m^2}F_3, \tag{B9b}$$

$$G_3 = F_3 + \frac{s}{c}F_2, \tag{B9c}$$

where $q_E^2 = \boldsymbol{q}^2 + q_4^2$ and $s \equiv \sin\alpha\cos\alpha$, $c \equiv \cos^2\alpha$.

For a given momentum transfer $\boldsymbol{q} = (q_1, q_2, q_3)$, Eqs. (B8) thus represent eight equations for $G_{1,2,3}$. They can be written in a compact form as follows:

$$K(q)\begin{pmatrix} G_1 \\ G_2 \\ G_3 \end{pmatrix} - V(q) = 0, \tag{B10}$$

where $K(q)$ is an 8×3 matrix given in block form by

$$K(q) = \begin{pmatrix} X_1(q) & 0 & X_3(q) \\ 0 & Y_1(q) & 0 \end{pmatrix}, \tag{B11a}$$

$$X_1(q) = m\begin{pmatrix} -cq_2 \\ cq_1 \\ s(E-m) \\ -isq_3 \end{pmatrix}, \tag{B11b}$$

$$X_3(q) = -\frac{c}{2}q_3\begin{pmatrix} q_1 \\ q_2 \\ q_3 \\ -i(E+m) \end{pmatrix}, \tag{B11c}$$

$$Y_1(q) = mc\begin{pmatrix} q_1 \\ q_2 \\ q_3 \\ -i(E+m) \end{pmatrix}, \tag{B11d}$$

and $V(q)$ is an eight-dimensional array given by

$$V(q) = \begin{pmatrix} V_R(q) \\ V_I(q) \end{pmatrix}, \tag{B12a}$$

$$V_R(q) = \begin{pmatrix} \mathrm{Re}\vec{\mathcal{V}}(q) \\ i\mathrm{Im}\mathcal{V}_4(q) \end{pmatrix}, \tag{B12b}$$

$$V_I(q) = \begin{pmatrix} \mathrm{Im}\vec{\mathcal{V}}(q) \\ -i\mathrm{Re}\mathcal{V}_4(q) \end{pmatrix}. \tag{B12c}$$

To solve for $G_{1,2,3}(q^2)$, for a given three-momentum transfer $\boldsymbol{q} = (q_1, q_2, q_3)$ we can use a least squares estimator. Namely, we minimize the function

$$F(G_{1,2,3}) = \sum_{\vec{q}\in P(\vec{q})}\sum_{i,j=1}^{8} w_{ij}(q)E_i(q)E_j(q), \tag{B13}$$

where

$$E_i(q) = \sum_{\beta=1}^{3} K_{i\beta}(q)G_\beta - V_i(q), \tag{B14}$$

$$w_{ij}(q) = [C_V^{-1}(q)]_{ij}, \tag{B15}$$

and the weights matrix is the inverse of the covariance matrix of lattice "measurements" $V_i(q)$:

$$[C_V(q)]_{ij} = \mathrm{Cov}(V_i(q), V_j(q)). \tag{B16}$$

For independent variables $V_i(q)$, the covariance matrix C_V and it inverse are positive definite.[9] This guarantees that $F(G_{1,2,3})$ is minimized if and only if $E_i(q) = 0$ for all i. The sum over momenta runs over the six permutations (q_1, q_2, q_3), (q_1, q_3, q_2), (q_2, q_1, q_3), (q_3, q_1, q_2), (q_2, q_3, q_1), and (q_3, q_2, q_1).

The function $F(G_{1,2,3})$ is stationary for

$$\frac{\partial F}{\partial G_\alpha} = 0, \qquad \alpha = 1, 2, 3. \tag{B17}$$

Explicitly, since $\partial E_j/\partial G_\alpha = K_{j\alpha}$, one finds

$$2\sum_{\vec{q}\in P(\vec{q})}\sum_{i,j=1}^{8} w_{ji}(q)E_i(q)K_{j\alpha}(q) = 0, \qquad \alpha = 1, 2, 3, \tag{B18}$$

or even more explicitly

$$\sum_{\vec{q}\in P(\vec{q})}\sum_{i,j=1}^{8} w_{ji}(q)\left(\sum_\beta K_{i\beta}(q)G_\beta - V_i(q)\right)K_{j\alpha}(q) = 0, \quad \alpha = 1, 2, 3, \tag{B19}$$

which is a system of three equations for $G_{1,2,3}$. The extremum condition for $F(G_{1,2,3})$ implies the following linear equation for $G_{1,2,3}(q^2)$:

$$A_{\alpha\beta}G_\beta = B_\alpha, \tag{B20}$$

where the 3×3 matrix A and the three-dimensional array B are given, respectively, by

[9] For ease of notation, we are ignoring current conservation, which relates the various components $V_i(q)$. Strictly speaking, we need to eliminate the dependent components of $V_i(q)$ when using a conserved current to get an invertible covariance matrix.

$$A_{\alpha\beta} = \sum_{\vec{q}\in P(\vec{q})} \sum_{i,j=1}^{8} K_{j\alpha}(q) w_{ji}(q) K_{i\beta}(q), \tag{B21a}$$

$$B_{\alpha} = \sum_{\vec{q}\in P(\vec{q})} \sum_{i,j=1}^{8} K_{j\alpha}(q) w_{ji}(q) V_{i}(q). \tag{B21b}$$

So, from the lattice data on $V_i(q)$, their covariance matrix, and the explicit form of the matrix $K_{i\alpha}(q)$ given in Eq. (B11), one can construct $A_{\alpha\beta}$ and B_α and solve for $G_{1,2,3}$. Error on $G_{1,2,3}$ can be assigned with the bootstrap method.

APPENDIX C: CHIRAL EXTRAPOLATION FORMULAS

We can express the electric dipole form factor as

$$\frac{F_3^i(q^2)}{2M_N} = d_i - S_i' q^2 + H_i(q^2), \tag{C1}$$

where d_i is the EDM, S_i' the Schiff moment (with some abuse of notation), and $H_i(q^2)$ account for the higher-order dependence on q^2. Here, i is an isospin label, and the results are more conveniently expressed in terms of an isoscalar ($i=0$) and isovector ($i=1$) component. The neutron and proton form factors are, respectively,

$$\begin{aligned} F_{3,p}(q^2) &= F_3^0(q^2) + F_3^1(q^2), \\ F_{3,n}(q^2) &= F_3^0(q^2) - F_3^1(q^2). \end{aligned} \tag{C2}$$

At NLO in χPT, the EDMs are given by [24,28,30,32]

$$d_0 = e\bar{d}_0 + \frac{e g_A \bar{g}_0}{(4\pi F_\pi)^2}\left[\frac{3\pi M_\pi}{4M_N}\right], \tag{C3}$$

$$d_1 = e\bar{d}_1(\mu) + \frac{e g_A \bar{g}_0}{(4\pi F_\pi)^2}\left[-\ln\frac{M_\pi^2}{\mu^2} + \frac{5\pi}{4}\frac{M_\pi}{M_N}\right], \tag{C4}$$

where the renormalization scale dependence of the low-energy constant $\bar{d}_1$ cancels the μ in the logarithm. Here $g_A = 1.27$ and $F_\pi = 92.4$ MeV. $\bar{g}_0$ is a $\cancel{CP}$ pion-nucleon coupling, defined as

$$\mathcal{L} = -\frac{\bar{g}_0}{2F_\pi}\bar{N}\boldsymbol{\pi}\cdot\boldsymbol{\tau}N, \tag{C5}$$

which is related by chiral symmetry to the neutron-proton mass splitting [24]

$$\bar{g}_0 = \left(\frac{M_n - M_p}{\bar{m}\varepsilon} + O\left(\frac{M_\pi^2}{\Lambda_\chi^2}\right)\right) m_* \bar{\Theta} = g_S \bar{m}\,\bar{\Theta}, \tag{C6}$$

where $m_*^{-1} = m_u^{-1} + m_d^{-1}$, $2\bar{m} = m_u + m_d$, and $\Lambda_\chi \sim 1$ GeV is the scale at which the χPT expansion breaks down. g_S is the isovector scalar charge, and the last equality holds in the isospin limit. At the physical pion mass, one obtains [76]

$$\frac{\bar{g}_0}{2F_\pi} = (15.5 \pm 2.6)\times 10^{-3}\bar{\Theta}, \tag{C7}$$

but the last term in Eq. (C6) allows the extension of the relation to arbitrary masses in the regime of validity of χPT. In particular, in the χPT fits to $F_3(q^2)$ we use

$$\bar{g}_0 = \frac{g_S}{2B} M_\pi^2 \bar{\Theta}, \tag{C8}$$

with $g_S = 1.0$ and $B = 2.8$ GeV. $\bar{d}_{0,1}$ are two low-energy constants, which, by naive-dimensional analysis, scale as

$$\bar{d}_{0,1} = \mathcal{O}\left(\frac{M_\pi^2}{(4\pi F_\pi)^3}\right). \tag{C9}$$

The first derivative of the form factor is [28,30,32]

$$S_0' = 0, \tag{C10}$$

$$S_1' = \frac{e g_A \bar{g}_0}{6(4\pi F_\pi)^2 M_\pi^2}\left[1 - \frac{5\pi}{4}\frac{M_\pi}{M_N}\right]. \tag{C11}$$

At N^2LO there are additional long- and short-distance contributions to both isoscalar and isovector components.

The remaining momentum dependence of the electric dipole form factor is given by the functions $H_i(q^2)$ introduced in Eq. (C1):

$$H_0(q^2) = 0, \tag{C12}$$

$$H_1(q^2) = \frac{4 e g_A \bar{g}_0}{15(4\pi F_\pi)^2}\left[h_a(x) - \frac{7\pi}{8}\frac{M_\pi}{M_N}h_b(x)\right], \tag{C13}$$

with $x \equiv q^2/4M_\pi^2$. h_a appears at leading order:

$$h_a(x) = -\frac{15}{4}\left[\sqrt{1+\frac{1}{x}}\ln\left(\frac{\sqrt{1+1/x}+1}{\sqrt{1+1/x}-1}\right) - 2\left(1+\frac{x}{3}\right)\right], \tag{C14}$$

while h_b is generated at NLO:

$$h_b(x) = -\frac{1}{7}\left[3(1+2x)\left(5\left(\frac{1}{\sqrt{x}}\arctan\sqrt{x} - 1 + \frac{x}{3}\right)\right) - 10x^2\right]. \tag{C15}$$

Since these behave as $h_i^{(n)}(x) = x^2 + \mathcal{O}(x^3)$ for $x \ll 1$, the leading, $O(q^4)$, dependence of H_i is consistent with the definition in Eq. (C1).

APPENDIX D: EXCITED-STATE CONTAMINATION IN CHIRAL PERTURBATION THEORY

In this appendix, we show that, in χPT, the gap between the ground-state and excited-state contributions to the CP-odd components of the three-point function $\mathcal{C}^{\mu}_{\rm 3pt}$ is expected to be of order of the pion mass M_π. This can be intuitively understood from the fact that the nucleon EDM induced by the QCD $\bar\Theta$-term receives a LO contribution from a long-range pion loop [24], shown in Fig. 22. In Minkowski space, this diagram has a branch cut when the intermediate pions and nucleon go on shell. In Euclidean space, this translates into a $N\pi$ excited state, whose amplitude is of the same size as the ground-state contribution. For simplicity, we focus only on the diagram shown in Fig. 22 and assume that the nucleon interpolating field does not couple to nucleon plus pions.

We start from the fourth component of the three-point function. Carrying out the Dirac traces in Eq. (25), in the limit $M_N \gg q$, we find

$$\begin{aligned}\mathcal{C}^4_{\rm 3pt} = {}& q_3\tau_3 \frac{\bar g_0 g_A}{(4\pi F_\pi)^2} e^{-M_N t_B - E_N t}\Bigg\{ f_0(M_\pi, q, L) \\ & + \frac{(4\pi)^2}{L^3 M_\pi E_\pi^2}\Bigg(e^{-M_\pi t} + e^{-M_\pi t_B} + \frac{E_\pi}{M_\pi}(e^{-E_\pi t} + e^{-E_\pi t_B}) \\ & - \frac{M_\pi + E_\pi}{2M_\pi}(e^{-E_\pi t - M_\pi t_B} + e^{-M_\pi t - E_\pi t_B}) \\ & + \frac{(E_\pi - m_\pi)^2}{2M_\pi(E_\pi + M_\pi)}(e^{-(M_\pi+E_\pi)t} + e^{-(M_\pi+E_\pi)t_B})\Bigg) \\ & + \cdots\Bigg\}, \end{aligned} \tag{D1}$$

where $t_B = \tau - t$, $E_N = \sqrt{M_N^2 + q^2} \sim M_N$, $E_\pi = \sqrt{M_\pi^2 + q^2}$ and $\cdots$ denotes terms with a gap with two or more units of momentum. $f_0(M_\pi, q, L)$ denotes the ground-state loop function, which we write as an infinite volume term f_0^∞ and a correction Δ:

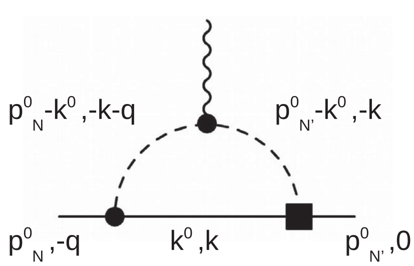

FIG. 22. Leading order diagram for the excited-state contribution to the three-point function $\mathcal{C}^{\mu}_{\rm 3pt}$ in chiral perturbation theory. A black square denotes an insertion of the CP-odd pion-nucleon couplings $\bar g_0$. Filled circles denote CP-even pion-nucleon and pion-photon couplings.

$$f_0(M_\pi, q, L) = f_0^\infty(M_\pi, q) + \Delta(M_\pi, q, L). \tag{D2}$$

In the nonrelativistic limit, $f_0^\infty(M_\pi, q)$ is given by

$$\begin{aligned} f_0^\infty(M_\pi, q) = (4\pi)^2\Bigg(\int \frac{d^4k}{(2\pi)^4}\frac{1}{k_0^2 + \vec k^2 + M_\pi^2} \\ \times \frac{1}{k_0^2 + (\vec k + \vec q)^2 + M_\pi^2}\Bigg) \end{aligned} \tag{D3}$$

and is ultraviolet divergent. In dimensional regularization and in the $\overline{\rm MS}$ scheme

$$f_0^\infty(M_\pi, q) = \log\frac{\mu^2}{M_\pi^2} + 2 - \sqrt{1 + \frac{1}{x}}\ln\frac{\sqrt{1+\frac{1}{x}}+1}{\sqrt{1+\frac{1}{x}}-1}, \tag{D4}$$

with $x = q^2/(4M_\pi^2)$, which is of course the same function as in Appendix C. The finite volume correction is given by

$$\begin{aligned}\Delta(M_\pi, q, L) = (4\pi)^2\int\frac{dk_0}{2\pi}\left(\frac{1}{L^3}\sum_{\vec k} - \int\frac{d^3k}{(2\pi)^3}\right) \\ \times \frac{1}{k_0^2 + \vec k^2 + M_\pi^2}\frac{1}{k_0^2 + (\vec k + \vec q)^2 + M_\pi^2}, \end{aligned} \tag{D5}$$

which can be written in terms of Bessel functions as [77]

$$\Delta(M_\pi, q, L) = 2\sum_{\vec n \neq 0}\int_0^1 dx K_0\left(L\sqrt{M_\pi^2 + q^2 x(1-x)}|\vec n|\right). \tag{D6}$$

At $q = 0$, for $M_\pi L \sim 4$, Δ amounts to a 0.1% correction. Equations (D1) and (D4) thus show that the excited states have a gap of $\mathcal{O}(M_\pi)$. The ratio of the ground- and excited-state contributions is determined by the quantity $(4\pi)^2/(LM_\pi)^3$, which is a number of order 1 for $LM_\pi = 4$. We thus do not expect a significant suppression of the excited states. A similar calculation can be performed for the spatial components $\mathcal{C}^i_{3pt}$, yielding a result similar to Eq. (D1), but with a sinh rather than a cosh behavior.

APPENDIX E: $O(a)$ CORRECTIONS IN THE WILSON-CLOVER THEORY

In this appendix, we analyze CP violation due to the topological charge in the Wilson-clover theory at $O(a)$. We will denote by $O_n^{(d)}$, $\tilde O_n^{(d)}$, and $O_n^{(d),\rm ren}$ the set of bare, subtracted, and renormalized operators of dimension d, respectively. Subtracted operators, i.e., operators free of power divergences, are defined by

$$\tilde{O}_{n'}^{(d)} = O_{n'}^{(d)} - \sum_{d'<d} \sum_{k} \frac{\beta_{n'k}^{(d)}}{a^{d-d'}} \tilde{O}_{k}^{(d')}, \tag{E1}$$

while finite (renormalized) operators are given by

$$O_{n}^{(d),\mathrm{ren}} = Z_{nn'} \tilde{O}_{n'}^{(d)}. \tag{E2}$$

The presence of $\tilde{O}_k^{(d')}$ and not $O_k^{(d')}$ in Eq. (E1) is needed to avoid ambiguities in the definition of lower-dimensional coefficients $\beta_{n'k}^{(d)}$. Note, however, that like all operators, the subtracted operators allow any amount of admixture of $a^{d'-d}\tilde{O}^{(d')}$ for $d' \geq d$.

We use the Wilson-clover quark action, in which the Dirac operator reads

$$O_D = D_L + m_W, \tag{E3}$$

$$D_L = \not{D} - a\left(\frac{r}{2} D^2 + \frac{r c_{\mathrm{SW}}}{4} \sigma \cdot G\right), \tag{E4}$$

with $c_{\mathrm{SW}} = 1 + O(g^2)$.[10] To simplify the analysis, in the following discussion we will first assume that the quark mass matrix is proportional to the identity, pointing out the minor modifications at the end.

The starting point of our analysis is the singlet axial Ward identity (AWI) obtained by considering the axial transformation on the quark fields $\psi^T = (u, d, s)$:

$$\begin{aligned} \psi(x) &\to (1 + i\alpha(x)\gamma_5)\psi(x), \\ \bar{\psi}(x) &\to \bar{\psi}(x)(1 + i\alpha(x)\gamma_5), \end{aligned} \tag{E5}$$

where $\alpha(x)$ is the local transformation parameter. Denoting by $O(x_1, \ldots, x_n)$ any product of local operators, the singlet AWI reads

$$\begin{aligned} &\langle O(x_1, \ldots, x_n)(\partial_x^\mu A_\mu(x) - 2m_W \bar{\psi}(x)\gamma_5\psi(x) - X(x))\rangle \\ &\quad = -\left\langle \frac{\delta O(x_1, \ldots, x_n)}{\delta(i\alpha(x))} \right\rangle, \end{aligned} \tag{E6}$$

where

$$A_\mu(x) = \bar{\psi}(x)\gamma_\mu\gamma_5\psi(x) \tag{E7}$$

and $X(x)$ is given by the variation of the Wilson-clover term [69,71,78]:

$$\frac{X}{2} = -a\bar{\psi}\left(\frac{r}{2} D^2 + \frac{r c_{\mathrm{SW}}}{4} \sigma \cdot G\right)\gamma_5 \psi. \tag{E8}$$

[10]Throughout, we use $D_\mu = \partial_\mu + iA_\mu$ and $G_{\mu\nu} = \partial_\mu A_\nu - \partial_\nu A_\mu + i[A_\mu, A_\nu]$, so that $[D_\mu, D_\nu] = iG_{\mu\nu}$ and $\not{D}\not{D} = D^2 + (1/2)\sigma \cdot G$.

Insertions of $X(x)$ vanish at tree level in the continuum limit, but quantum effects induce power-divergent mixing with lower-dimensional operators, that have to be taken into account when taking the continuum limit. This is done by writing [69,71,78]

$$\begin{aligned} X(x) = {}& a\tilde{X}(x) - 2\bar{m}\,\bar{\psi}(x)\gamma_5\psi(x) - (Z_A - 1)\partial_x^\mu A_\mu(x) \\ &+ Z_{G\tilde{G}} \frac{2N_F}{32\pi^2} (G\tilde{G})_{\mathrm{sub}}, \end{aligned} \tag{E9}$$

where N_F is the number of quark flavors and $\tilde{X}(x)$ is a "subtracted" dimension-five operator; i.e., it is free of power divergences, expanded according to Eq. (E1). The operator $a\tilde{X}(x)$ has no impact on the analysis of the axial WI with elementary fields, while it induces contact terms in the continuum limit of axial WIs involving composite fields [69,70]. It is, however, essential in order to identify the $O(a)$ corrections to $d_n(\bar{\Theta})$. Using the above expression in (E6) and taking into account the mixing between $(G\tilde{G})$ and $\partial_\mu A^\mu$ (which involves the renormalization constant Z_C), one arrives at [70,71]

$$\begin{aligned} &\bigg\langle O(x_1, \ldots, x_n)(Z_A(1 - Z_C)\partial_x^\mu A_\mu(x) - 2m\bar{\psi}(x)\gamma_5\psi(x) \\ &\quad - \frac{2N_F}{32\pi^2}(G\tilde{G})_{\mathrm{ren}} - a\tilde{X}(x))\bigg\rangle = -\left\langle \frac{\delta O(x_1, \ldots, x_n)}{\delta(i\alpha(x))} \right\rangle, \end{aligned} \tag{E10}$$

where

$$m = m_W - \bar{m} \tag{E11}$$

is the quark mass free of power divergences as we take the continuum limit. Here, and henceforth, the $O(ma)$ dependence of the coefficients of the operators is suppressed. Finally, upon integrating over $\int d^4x$ we arrive at

$$\begin{aligned} &\int d^4x \bigg\langle O(x_1, \ldots, x_n)\bigg(-2m\bar{\psi}(x)\gamma_5\psi(x) \\ &\quad - \frac{2N_F}{32\pi^2}(G\tilde{G})_{\mathrm{ren}} - a\tilde{X}(x)\bigg)\bigg\rangle \\ &\quad = -\int d^4x \left\langle \frac{\delta O(x_1, \ldots, x_n)}{\delta(i\alpha(x))} \right\rangle. \end{aligned} \tag{E12}$$

Reference [79] performed a detailed diagrammatic analysis of Eq. (E12), with $O(x_1, x_2.x_3) = N(x_1)J_\mu^{\mathrm{EM}}(x_2)\bar{N}(x_3)$ in the $a \to 0$ case, showing that the δO terms cancel the connected insertions of $2m\bar{\psi}\gamma_5\psi$. Their analysis shows that insertions of the operator $G\tilde{G}$ can be replaced by $2m$ times the disconnected insertions of the isosinglet pseudoscalar density $\bar{\psi}\gamma_5\psi$. Since the disconnected matrix elements of the isoscalar density do not diverge in the chiral limit, this implies as a corollary that the neutron EDM should vanish as $m \to 0$. $O(a)$ effects would modify the result of Ref. [79] by modifying the rhs of their Eqs. (2.11) and (3.5). In the context of our analysis, the term proportional to $a\tilde{X}$ in Eq. (E12) provides $O(a)$ effects, which we discuss next.

First, we project the subtracted operator $\tilde{X}$ on the basis of (subtracted) dim-5 operators, given in Ref. [80],

$$\tilde{X} = \sum_n K_{Xn} \tilde{O}_n^{(5)} \tag{E13}$$

and analyze the consequences of Eq. (E13) for Eq. (E12). The basis of dimension-5 operators $O_n^{(5)}$ appearing on the rhs of Eq. (E13) is given in [80] assuming generic diagonal quark mass $\hat{m}$, and we repeat it here for completeness:

$$O_1^{(5)} = i\bar{\psi}\tilde{\sigma}^{\mu\nu} G_{\mu\nu}\psi, \tag{E14}$$

$$O_2^{(5)} = \partial^2(\bar{\psi} i\gamma_5\psi), \tag{E15}$$

$$O_3^{(5)} = ie\bar{\psi}\tilde{\sigma}^{\mu\nu} Q F_{\mu\nu}\psi, \tag{E16}$$

$$O_4^{(5)} = \mathrm{Tr}[\hat{m}Q^2]\frac{1}{2}\epsilon^{\mu\nu\alpha\beta}F_{\mu\nu}F_{\alpha\beta}, \tag{E17}$$

$$O_5^{(5)} = \mathrm{Tr}[\hat{m}]\frac{1}{2}\epsilon^{\mu\nu\alpha\beta}G^b_{\mu\nu}G^b_{\alpha\beta}, \tag{E18}$$

$$O_6^{(5)} = \mathrm{Tr}[\hat{m}]\partial_\mu(\bar{\psi}\gamma^\mu\gamma_5\psi), \tag{E19}$$

$$O_7^{(5)} = \partial_\mu(\bar{\psi}\gamma^\mu\gamma_5\hat{m}\psi) - \frac{1}{3}\mathrm{Tr}[\hat{m}]\partial_\mu(\bar{\psi}\gamma^\mu\gamma_5\psi), \tag{E20}$$

$$O_8^{(5)} = \bar{\psi} i\gamma_5 \hat{m}^2\psi, \tag{E21}$$

$$O_9^{(5)} = \mathrm{Tr}[\hat{m}^2]\bar{\psi} i\gamma_5\psi, \tag{E22}$$

$$O_{10}^{(5)} = \mathrm{Tr}[\hat{m}]\bar{\psi} i\gamma_5\hat{m}\psi, \tag{E23}$$

$$O_{11}^{(5)} \equiv P_{EE} = i\bar{\psi}_E\gamma_5\psi_E, \tag{E24}$$

$$O_{12}^{(5)} \equiv \partial\cdot A_E = \partial_\mu[\bar{\psi}_E\gamma^\mu\gamma_5\psi + \bar{\psi}\gamma^\mu\gamma_5\psi_E], \tag{E25}$$

$$O_{13}^{(5)} \equiv A_\partial = \bar{\psi}\gamma_5\not{\partial}\psi_E - \bar{\psi}_E\overleftarrow{\not{\partial}}\gamma_5\psi, \tag{E26}$$

$$O_{14}^{(5)} \equiv A_{A^{(\gamma)}} = ie(\bar{\psi}Q\not{A}^{(\gamma)}\gamma_5\psi_E - \bar{\psi}_E Q\not{A}^{(\gamma)}\gamma_5\psi), \tag{E27}$$

where $\tilde{\sigma}^{\mu\nu} \equiv \frac{1}{2}(\sigma^{\mu\nu}\gamma_5 + \gamma_5\sigma^{\mu\nu})$ and $\psi_E = (\not{D} + \hat{m})\psi$.

Keeping in mind that $O(x_1, \ldots, x_n)$ has the structure $N(x_1)J_\mu^{\mathrm{EM}}(x_2)\bar{N}(x_3)$, in terms of the neutron source and sink operator and the electromagnetic current, the various $O_n^{(5)}$ contribute to Eq. (E12) as follows.

(i) $O_1^{(5)}$ is the isoscalar chromo-EDM operator and contributes an $O(a)$ term to the lhs of Eq. (E12). In fact, as shown below, this is the leading $O(a)$ contribution, thus proving a linear relation between isovector insertions of the pseudoscalar density and the chromo-EDM.

(ii) $O_{2,6,7}^{(5)}$ are total derivatives and their insertion in Eq. (E12) vanishes upon integration over $\int d^4x$.

(iii) $O_{3,4}^{(5)}$ involve one and two powers of the electromagnetic field strength. In order to eliminate the photon field in the correlation functions in Eq. (E12), one needs electromagnetic loops, making the contribution of $O_{3,4}^{(5)}$ to Eq. (E12) of $O(a\alpha_{\mathrm{EM}}/\pi)$ and thus negligible to the order we are working.

(iv) $O_5^{(5)}$ provides a correction of $O(am)$ proportional to $(G\tilde{G})$ in the lhs of Eq. (E12).

(v) $O_{8,9,10}^{(5)}$ become $\hat{m}^2\bar{\psi}i\gamma_5\psi$ when $\hat{m} \propto I$. Therefore, their contributions have the same form of the pseudoscalar insertion in Eq. (E12) but suppressed by $O(am)$.

(vi) The operators $O_{11,12,13,14}^{(5)}$ vanish by using the quark equations of motion and can contribute contact terms to the lhs of Eq. (E12). However, it turns out that none of them actually contributes at this order. $O_{11}^{(5)}$ contains two equation of motion operators. Therefore, when inserted in Eq. (E12), it will always involve a contraction with a quark field in the neutron source or sink operator, and thus it will not contribute to the residue of the neutron pole. $O_{12}^{(5)}$ is a total derivative and drops out of Eq. (E12). $O_{13}^{(5)}$ is a gauge-variant operator and drops out of Eq. (E12) as long as $O(x_1, \ldots, x_n)$ is a gauge singlet, which is the case for $O(x_1, x_2, x_4) \propto N(x_1)J_\mu^{\mathrm{EM}}(x_2)\bar{N}(x_3)$. $O_{14}^{(5)}$ involves the photon field and therefore can contribute to Eq. (E12) only to $O(a\alpha_{\mathrm{EM}}/\pi)$.

So in summary, for $\hat{m} \propto I$, Eq. (E12) becomes

$$\begin{aligned}\int d^4x \Big\langle & O(x_1, \ldots, x_n)(-2m\bar{\psi}(x)\gamma_5\psi(x)(1 + O(am)) \\ & - \frac{2N_F}{32\pi^2}(G\tilde{G})_{\mathrm{ren}}(1 + O(am)) - aK_{X1}\tilde{O}_1^{(5)})\Big\rangle \\ & = -\int d^4x \langle \frac{\delta O(x_1, \ldots, x_n)}{\delta(i\alpha(x))}\rangle. \end{aligned} \tag{E28}$$

If $\hat{m} \neq I$, the singlet AWI, Eq. (E12), involves $\bar{\psi}\,\hat{m}\,\gamma_5\psi$. All the arguments above go through, except for the effect of $O_{8,9,10}^{(5)}$. $O_{10}^{(5)}$ gives a correction of $O(am)$ proportional to $\bar{\psi}\,\hat{m}\,\gamma_5\psi$, while $O_{8,9}^{(5)}$ contribute nonmultiplicative terms involving the nonsinglet pseudoscalar densities of $O(a\hat{m}^2)$ in Eq. (E28). The presence of these additional terms does not affect our conclusion about the existence of $O(am_q^0)$ corrections.

[1] M. Pospelov and A. Ritz, Ann. Phys. (Amsterdam) **318**, 119 (2005).
[2] J. Engel, M. J. Ramsey-Musolf, and U. van Kolck, Prog. Part. Nucl. Phys. **71**, 21 (2013).
[3] C. L. Bennett *et al.* (WMAP Collaboration), Astrophys. J. Suppl. **148**, 1 (2003).
[4] E. W. Kolb and M. S. Turner, *The Early Universe*, Frontiers in Physics Vol. 69 (1990), ISBN 978-0-201-62674-2.
[5] P. Coppi, eConf **C040802**, L017 (2004), https://www.slac.stanford.edu/econf/C040802/papers/L017.PDF.
[6] A. D. Sakharov, Pis'ma Zh. Eksp. Teor. Fiz. **5**, 32 (1967) [JETP Lett. **5**, 24 (1967)], http://jetpletters.ru/ps/1643/article_25089.shtml.
[7] M. Kobayashi and T. Maskawa, Prog. Theor. Phys. **49**, 652 (1973).
[8] Z. Maki, M. Nakagawa, and S. Sakata, Prog. Theor. Phys. **28**, 870 (1962).
[9] H. Nunokawa, S. J. Parke, and J. W. F. Valle, Prog. Part. Nucl. Phys. **60**, 338 (2008).
[10] I. B. Khriplovich and A. R. Zhitnitsky, Phys. Lett. **109B**, 490 (1982).
[11] A. Czarnecki and B. Krause, Phys. Rev. Lett. **78**, 4339 (1997).
[12] C.-Y. Seng, Phys. Rev. C **91**, 025502 (2015).
[13] C. Abel *et al.* (nEDM Collaboration), Phys. Rev. Lett. **124**, 081803 (2020).
[14] B. Graner, Y. Chen, E. G. Lindahl, and B. R. Heckel, Phys. Rev. Lett. **116**, 161601 (2016); **119**, 119901(E) (2017).
[15] T. Ito, SNS nEDM progress and plans, https://indico.frib.msu.edu/event/13/contributions/191/attachments/79/384/SNSnEDM_Ito.pdf (2019).
[16] R. Jackiw and C. Rebbi, Phys. Rev. Lett. **37**, 172 (1976).
[17] C. G. Callan, Jr., R. F. Dashen, and D. J. Gross, Phys. Lett. **63B**, 334 (1976).
[18] D. J. Gross, R. D. Pisarski, and L. G. Yaffe, Rev. Mod. Phys. **53**, 43 (1981).
[19] A. D. Dolgov, Phys. Rep. **222**, 309 (1992).
[20] V. A. Kuzmin, M. E. Shaposhnikov, and I. I. Tkachev, Phys. Rev. D **45**, 466 (1992).
[21] I. I. Y. Bigi and N. G. Uraltsev, Nucl. Phys. **B353**, 321 (1991).
[22] M. Pospelov and A. Ritz, Phys. Rev. Lett. **83**, 2526 (1999).
[23] R. D. Peccei and H. R. Quinn, Phys. Rev. Lett. **38**, 1440 (1977).
[24] R. J. Crewther, P. Di Vecchia, G. Veneziano, and E. Witten, Phys. Lett. **88B**, 123 (1979); **91B**, 487(E) (1980).
[25] A. Pich and E. de Rafael, Nucl. Phys. **B367**, 313 (1991).
[26] P. L. Cho, Phys. Rev. D **48**, 3304 (1993).
[27] B. Borasoy, Phys. Rev. D **61**, 114017 (2000).
[28] W. H. Hockings and U. van Kolck, Phys. Lett. B **605**, 273 (2005).
[29] S. Narison, Phys. Lett. B **666**, 455 (2008).
[30] K. Ottnad, B. Kubis, U.-G. Meißner, and F.-K. Guo, Phys. Lett. B **687**, 42 (2010).
[31] J. de Vries, E. Mereghetti, R. G. E. Timmermans, and U. van Kolck, Phys. Lett. B **695**, 268 (2011).
[32] E. Mereghetti, J. de Vries, W. H. Hockings, C. M. Maekawa, and U. van Kolck, Phys. Lett. B **696**, 97 (2011).
[33] M. Pospelov and A. Ritz, Phys. Rev. D **63**, 073015 (2001).
[34] O. Lebedev, K. A. Olive, M. Pospelov, and A. Ritz, Phys. Rev. D **70**, 016003 (2004).
[35] K. Fuyuto, J. Hisano, and N. Nagata, Phys. Rev. D **87**, 054018 (2013).
[36] U. Haisch and A. Hala, J. High Energy Phys. 11 (2019) 154.
[37] E. Shintani, S. Aoki, N. Ishizuka, K. Kanaya, Y. Kikukawa, Y. Kuramashi, M. Okawa, Y. Taniguchi, A. Ukawa, and T. Yoshié, Phys. Rev. D **72**, 014504 (2005).
[38] F. Berruto, T. Blum, K. Orginos, and A. Soni, Phys. Rev. D **73**, 054509 (2006).
[39] A. Shindler, J. de Vries, and T. Luu, Proc. Sci., LATTICE2014 (**2014**) 251 [arXiv:1409.2735].
[40] F.-K. Guo, R. Horsley, U.-G. Meißner, Y. Nakamura, H. Perlt, P. E. L. Rakow, G. Schierholz, A. Schiller, and J. M. Zanotti, Phys. Rev. Lett. **115**, 062001 (2015).
[41] A. Shindler, T. Luu, and J. de Vries, Phys. Rev. D **92**, 094518 (2015).
[42] C. Alexandrou, A. Athenodorou, M. Constantinou, K. Hadjiyiannakou, K. Jansen, G. Koutsou, K. Ottnad, and M. Petschlies, Phys. Rev. D **93**, 074503 (2016).
[43] E. Shintani, T. Blum, T. Izubuchi, and A. Soni, Phys. Rev. D **93**, 094503 (2016).
[44] J. Dragos, T. Luu, A. Shindler, J. de Vries, and A. Yousif, Phys. Rev. C **103**, 015202 (2021).
[45] T. Bhattacharya, V. Cirigliano, R. Gupta, H.-W. Lin, and B. Yoon, Phys. Rev. Lett. **115**, 212002 (2015).
[46] R. Gupta, B. Yoon, T. Bhattacharya, V. Cirigliano, Y.-C. Jang, and H.-W. Lin, Phys. Rev. D **98**, 091501(R) (2018).
[47] M. Abramczyk, S. Aoki, T. Blum, T. Izubuchi, H. Ohki, and S. Syritsyn, Phys. Rev. D **96**, 014501 (2017).
[48] T. Bhattacharya, B. Yoon, R. Gupta, and V. Cirigliano, Proc. Sci. LATTICE2018 (**2019**) 188.
[49] J. Kim, J. Dragos, A. Shindler, T. Luu, and J. de Vries, Proc. Sci., LATTICE2018 (**2019**) 260 [arXiv:1810.10301].
[50] C. Alexandrou, S. Bacchio, M. Constantinou, J. Finkenrath, K. Hadjiyiannakou, K. Jansen, G. Koutsou, and A. V. Aviles-Casco, Phys. Rev. D **100**, 014509 (2019).
[51] A. Bazavov *et al.* (MILC Collaboration), Phys. Rev. D **87**, 054505 (2013).
[52] R. Gupta, Y.-C. Jang, B. Yoon, H.-W. Lin, V. Cirigliano, and T. Bhattacharya, Phys. Rev. D **98**, 034503 (2018).
[53] Y.-C. Jang, R. Gupta, H.-W. Lin, B. Yoon, and T. Bhattacharya, Phys. Rev. D **101**, 014507 (2020).
[54] M. Lüscher, J. High Energy Phys. 08 (2010) 071; 03 (2014) 092(E).
[55] E. Witten, Nucl. Phys. **B156**, 269 (1979).
[56] G. Veneziano, Nucl. Phys. **B159**, 213 (1979).
[57] N. J. Evans, S. D. H. Hsu, and M. Schwetz, Phys. Lett. B **382**, 138 (1996).
[58] R. J. Crewther, Phys. Lett. **70B**, 349 (1977).
[59] P. Di Vecchia and G. Veneziano, Nucl. Phys. **B171**, 253 (1980).
[60] H. Leutwyler and A. V. Smilga, Phys. Rev. D **46**, 5607 (1992).
[61] C. Bernard and D. Toussaint (MILC Collaboration), Phys. Rev. D **97**, 074502 (2018).
[62] C. Alexandrou, A. Athenodorou, K. Cichy, A. Dromard, E. Garcia-Ramos, K. Jansen, U. Wenger, and F. Zimmermann, Eur. Phys. J. C **80**, 424 (2020).

[63] M. Lüscher and F. Palombi, J. High Energy Phys. 09 (2010) 110.
[64] L. Giusti and M. Lüscher, J. High Energy Phys. 03 (2009) 013.
[65] K.-F. Liu, J. Liang, and Y.-B. Yang, Phys. Rev. D **97**, 034507 (2018).
[66] S. Syritsyn, T. Izubuchi, and H. Ohki, Proc. Sci., Confinement2018 (**2019**) 194 [arXiv:1901.05455].
[67] B. Yoon, T. Bhattacharya, V. Cirigliano, and R. Gupta, Proc. Sci., LATTICE2019 (**2020**) 243 [arXiv:2003.05390].
[68] T. Bhattacharya, R. Gupta, W. Lee, S. R. Sharpe, and J. M. S. Wu, Phys. Rev. D **73**, 034504 (2006).
[69] M. Bochicchio, L. Maiani, G. Martinelli, G. C. Rossi, and M. Testa, Nucl. Phys. **B262**, 331 (1985).
[70] M. Testa, J. High Energy Phys. 04 (1998) 002.
[71] D. Guadagnoli and S. Simula, Nucl. Phys. **B670**, 264 (2003); **B906**, 615 (2016).
[72] C. Alexandrou, A. Athenodorou, K. Hadjiyiannakou, and A. Todaro, Phys. Rev. D **103**, 054501 (2021).
[73] R. G. Edwards and B. Joo (SciDAC Collaboration, LHPC Collaboration, UKQCD Collaboration), Nucl. Phys. B, Proc. Suppl. **140**, 832 (2005).
[74] T. A. DeGrand and P. Rossi, Comput. Phys. Commun. **60**, 211 (1990).
[75] M. E. Peskin and D. V. Schroeder, *An Introduction to Quantum Field Theory* (Addison-Wesley, Reading, MA, 1995).
[76] J. de Vries, E. Mereghetti, and A. Walker-Loud, Phys. Rev. C **92**, 045201 (2015).
[77] S. R. Beane, Phys. Rev. D **70**, 034507 (2004).
[78] L. H. Karsten and J. Smit, Nucl. Phys. **B183**, 103 (1981).
[79] D. Guadagnoli, V. Lubicz, G. Martinelli, and S. Simula, J. High Energy Phys. 04 (2003) 019.
[80] T. Bhattacharya, V. Cirigliano, R. Gupta, E. Mereghetti, and B. Yoon, Phys. Rev. D **92**, 114026 (2015).